

Finite-time thermodynamic bounds and tradeoff relations for information processing

Takuya Kamijima,^{1,*} Ken Funo,¹ and Takahiro Sagawa^{1,2}

¹*Department of Applied Physics, The University of Tokyo, 7-3-1 Hongo, Bunkyo-ku, Tokyo 113-8656, Japan*

²*Quantum-Phase Electronics Center (QPEC), The University of Tokyo, 7-3-1 Hongo, Bunkyo-ku, Tokyo 113-8656, Japan*

In thermal environments, information processing requires thermodynamic costs determined by the second law of thermodynamics. Information processing within finite time is particularly important, since fast information processing has practical significance but is inevitably accompanied by additional dissipation. In this paper, we reveal the fundamental thermodynamic costs and the tradeoff relations between incompatible information processing such as measurement and feedback in the finite-time regime. To this end, we introduce a general framework based on the concept of the Pareto front for thermodynamic costs, revealing the existence of fundamental tradeoff relations between them. Focusing on discrete Markov jump processes, we consider the tradeoff relation between thermodynamic activities, which in turn determines the tradeoff relation between entropy productions. To identify the Pareto fronts, we introduce a new Wasserstein distance that captures the thermodynamic costs of subsystems, providing a geometrical perspective on their structure. Our framework enables us to find the optimal entropy production of subsystems and the optimal time evolution to realize it. In an illustrative example, we find that even in situations where naive optimization of total dissipation cannot realize the function of Maxwell's demon, reduction of the dissipation in the feedback system according to the tradeoff relation enables the realization of the demon. We also show that an optimal Maxwell's demon can be implemented by using double quantum dots. Furthermore, our framework is applicable to larger scale systems with multiple states, as demonstrated by a model of chemotaxis. Our results would serve as a designing principle of efficient thermodynamic machines performing information processing, from single electron devices to biochemical signal transduction.

I. INTRODUCTION

A. Background

With advancements in measurement and control techniques in microscopic systems, stochastic thermodynamics has seen progress in both theoretical and experimental aspects over the past few decades [1–4]. Although the second law of thermodynamics has been well established, the maximum efficiency can only be achieved in infinite time (i.e., the quasi-static limit). Therefore, exploring thermodynamic bounds in the finite-time regime has become a topic of active research [5–12], especially in terms of thermodynamic speed limit [13–17] and thermodynamic uncertainty relations [18–30]. The central problem is estimating the additional entropy production (EP) that accompanies finite-time thermodynamic processes, compared to the infinite-time limit. In particular, it has been revealed that optimal transport theory [31, 32] provides the minimum amount of EP in finite-time processes for both overdamped Langevin systems [33–36] and discrete systems [37–40], where the optimal thermodynamic cost can always be achieved by designing optimal protocols for any finite time interval. The Landauer principle [41–46] for finite-time information erasure has been addressed by this approach [47–51], but more general information processing in finite time remains elusive.

In general, information plays a central role in thermodynamics [52], as illustrated by a thought experiment of “Maxwell's demon” [53]. A typical setup consists of mea-

surement and feedback as shown in Fig. 2, where subsystem Y (the memory of a demon) performs measurement and feedback on subsystem X (the engine). As in this example, cooperative behavior of subsystems enables information processing and work extraction. In recent decades, the fundamental energy costs (or the extractable work) in such information processing processes have been revealed from the perspective of the generalized second law of thermodynamics [54–61].

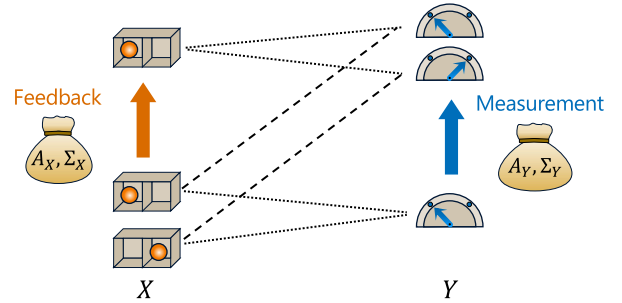


FIG. 2. A schematic of the simplest setup for measurement and feedback. Subsystem Y serves as the memory and measures subsystem X , which functions as the engine. Based on the measurement results, X receives feedback. Both the measurement and feedback processes, performed in finite time, require the thermodynamic costs such as activities A_X, A_Y and entropy productions Σ_X, Σ_Y . The overall time evolution is divided into separate steps of measurement and feedback, allowing X and Y to be considered as evolving partially in time. We however emphasize that our theoretical framework developed in this paper is applicable to a broader class of information processing, where the measurement and feedback steps are not necessarily temporally separated.

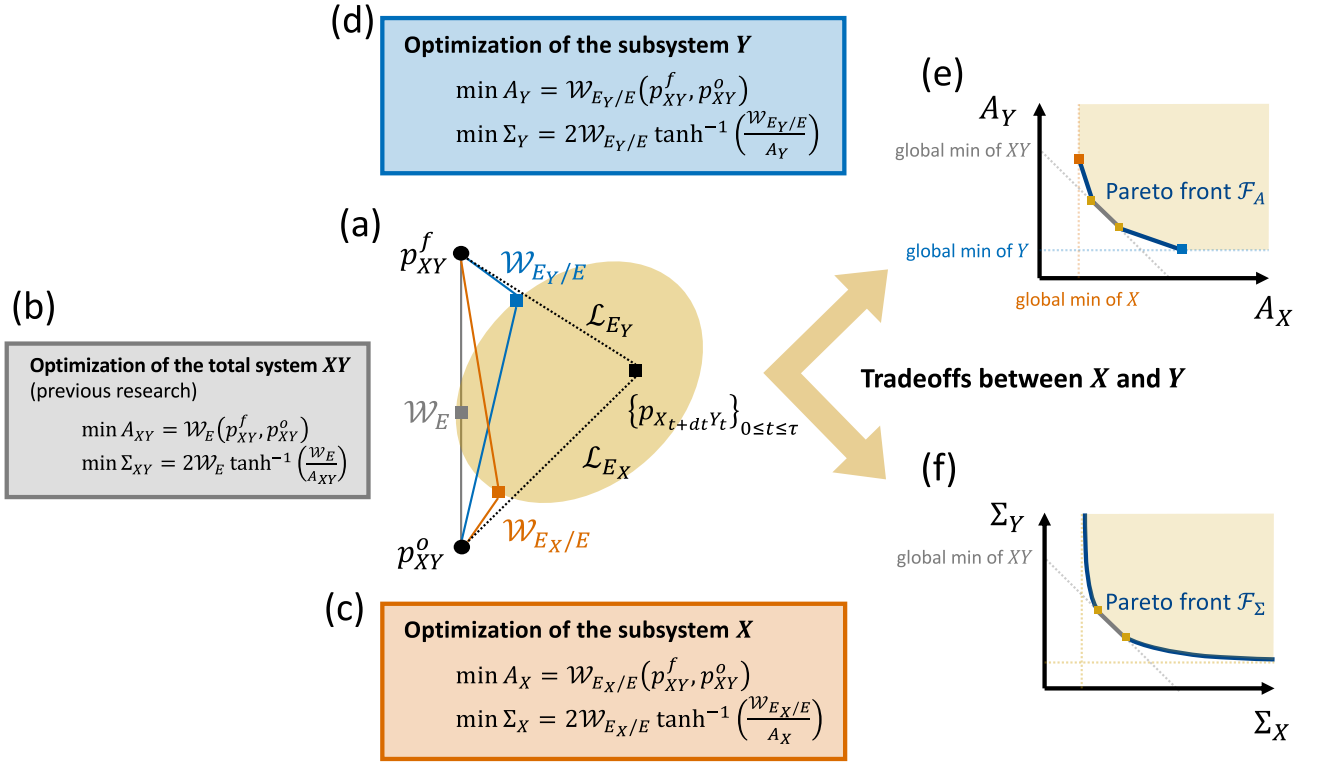


FIG. 1. The summary of main results and visualization of the origin of the thermodynamic tradeoff relations. (a) The central schematic diagram illustrates the difference between local and global optimization using partial time evolution (black squares). Partial time evolution specifies the extent to which the transition rates of subsystems (such as the memory and the engine) contribute to the overall time evolution (see Fig. 2 and Eqs. (12)(13)). In local optimization, the black square is fixed, and the transition rates within each subsystem are optimized. The length \mathcal{L}_{E_X} (\mathcal{L}_{E_Y}) from the initial distribution p_{XY}^o (final distribution p_{XY}^f) to the black square represents the local minimum of the partial activity for X (Y). In global optimization, this partial time evolution is optimized as well. The yellow area in the figure schematically represents the range within which the black square can be taken. By choosing the time evolution represented by the gray square, the total activity can reach the minimum value [38] (gray box (b)). To globally minimize the partial activity of X, one should choose the time evolution represented by the orange square. Conversely, selecting the blue square will globally minimize the partial activity of Y. (c)(d) The orange and blue boxes represent the global minimum thermodynamic costs of subsystems X and Y, respectively, during the time evolution $p_{XY}^o \rightarrow p_{XY}^f$. Since the partial time evolutions (orange and blue squares) that realize these two minima generally do not coincide, it is not possible to simultaneously achieve the minimum activity or dissipation for subsystems X and Y. Therefore, there exist tradeoff relations between these thermodynamic costs. (e)(f) The schematic diagrams on the right represent the typical tradeoff relation between the activities of the subsystems, as well as between the dissipations of the subsystems. The yellow-shaded areas in the diagrams represent the feasible regions of thermodynamic costs, and the lower left polyline and curved line indicate the optimal bounds (Pareto fronts \mathcal{F}_A and \mathcal{F}_Σ).

However, the thermodynamic costs for Maxwell's setups, including processes such as measurement and feedback, in finite time have been rarely addressed [36, 62–65] and yet to be understood. In fact, optimal transport theory cannot be directly applied to subsystems such as the memory and engine, while as mentioned before, the thermodynamic costs such as thermodynamic activity and EP for the total system have recently been studied in terms of optimal transport theory.

B. Summary of the Results

In this paper, we explore the fundamental bounds of thermodynamic costs for information processing in finite time.

To this end, we introduce a general framework based on the concept of the Pareto front for thermodynamic costs to characterize the tradeoff relations between them. Based on this framework, we reveal that there exist tradeoff relations for both entropy productions and thermodynamic activities. To determine the Pareto fronts, we generalize optimal transport theory by newly introducing a Wasserstein pseudo-distance associated with subsystems. Applying our framework to a measurement and feedback setting, we demonstrate that the thermodynamic costs required for measurement and feedback are incompatible. We then apply our framework to a simple model of information processing, elucidating a design principle of Maxwell's demon. Furthermore, we demonstrate that our framework can determine the optimal thermodynamic

costs even in more complex systems, exemplified by a model of chemotaxis.

Below, we briefly summarize our results of this paper, which are schematically shown in Fig. 1. We focus on Markov jump processes as a theoretical description of thermodynamic processes. The transition rates are manipulated over a finite operation time τ to evolve the system from the initial distribution p_{XY}^o to the final distribution p_{XY}^f . The transition rates of the total system are defined only on the edge set E , which consists of the edge sets E_X and E_Y of subsystems X and Y . Figure 1(a) illustrates the differences in local and global optimizations and the origin of the tradeoff relations in thermodynamic costs. For these optimizations, we introduce the concept of partial time evolution, as illustrated in Fig. 2. In this setting, the time evolution of the total system can be decomposed into changes in subsystems X and Y , corresponding to measurement and feedback, respectively. Such a decomposition can also be specified at each time point if we consider an infinitesimal time step, referred to as partial time evolution $p_{X_t Y_t} \rightarrow p_{X_{t+dt} Y_t}, p_{X_t Y_{t+dt}}$ ($0 \leq t \leq \tau$). In other words, $p_{X_{t+dt} Y_t}$ describes how subsystem X contributes to the overall time evolution, given $p_{X_t Y_t} \rightarrow p_{X_{t+dt} Y_{t+dt}}$ (see Eqs. (12)(13) for definition). The black square in Fig. 1(a) represents one such partial time evolution. The yellow-shaded area schematically represents the set of possible partial time evolutions.

In Sec. III A, we perform local optimization of the thermodynamic costs of the subsystems. To achieve this, we fix a specific partial time evolution $p_{X_t Y_t} \rightarrow p_{X_{t+dt} Y_t}, p_{X_t Y_{t+dt}}$ ($0 \leq t \leq \tau$). From the perspective of information processing, this specifies the information exchange between subsystems, determining whether X or Y performs measurement or feedback at each moment. In this scenario, we can optimize the transition rates R_X (R_Y) during the partial time evolution $p_{X_t Y_t} \rightarrow p_{X_{t+dt} Y_t}$ ($p_{X_t Y_t} \rightarrow p_{X_t Y_{t+dt}}$) to minimize the thermodynamic costs of subsystem X (Y). The minimal cost obtained through this optimization is feasible for each subsystem, and we refer to this as *local optimization* in this paper. In Fig. 1(a), the length \mathcal{L}_{E_X} (\mathcal{L}_{E_Y}) from the initial distribution p_{XY}^o (final distribution p_{XY}^f) to the black square represents the partial activity required for X (Y) during this time evolution (see Eq. (14)). Using these, the minimal partial EPs can also be determined (see Eq. (15)). However, since there is still room to optimize the partial time evolutions $p_{X_{t+dt} Y_t}$ and $p_{X_t Y_{t+dt}}$, these minimum values can potentially be further reduced.

In Sec. III B, we perform global optimization of the thermodynamic costs for the subsystems. This optimization involves not only the procedures of local optimization but also optimizing the partial time evolutions. This corresponds to moving the black square (partial time evolution) within the

yellow-shaded area in Fig. 1(a). Therefore, to minimize the partial activity of X , one should choose the time evolution (orange square) that minimizes \mathcal{L}_{E_X} . This optimization involves adjusting the Y component of the transition rates, R_Y , thereby optimizing the overall transition rates, R . Physically, this means selecting the interactions between X and Y such that the changes in X are minimized. We refer to this as *global optimization* in this paper. We generalize the Wasserstein distance to solve this optimization. The global minimum of the partial activity for X is given by the first equation in Fig. 1(c) (see Eq. (19)). Conversely, the global minimum of the partial EP for X is given by the second equation in Fig. 1(c) (see Eq. (21)). To ensure that the timescale of X 's dynamics remains finite, we set an upper bound A_X on X 's partial activity. Similarly, global optimization can be performed for Y (see Fig. 1(d)).

The global minimum costs for X and Y in general cannot be achieved simultaneously. This is because the protocols that realize these minimum costs are distinct between X and Y . This discrepancy arises from the different preferences in partial time evolution (represented by the orange and blue squares in Fig. 1(a)). Consequently, there exist tradeoff relations between the thermodynamic costs for X and Y .

In Sec. IV, we determine the bounds of the tradeoff relations between the thermodynamic costs of subsystems X and Y . The bounds of such tradeoff relations can be explicitly represented by the Pareto front, which is the set of optimal cost combinations (see Sec. IV A). We derive the Pareto front of partial activities in Sec. IV B, based on which we derive the Pareto front of partial EPs in Sec. IV C. Similar to global optimization, obtaining the Pareto front \mathcal{F}_A of the partial activities requires optimizing the partial time evolutions, which reduces to solving an optimal transport problem. In general, \mathcal{F}_A forms a convex polyline with a finite number of vertices and edges (see Fig. 1(e)). A vertex appears when the solution to the optimal transport problem is unique, whereas an edge appears when it is not. Along the edges, the operational speed required for time evolution can be adjusted between subsystems. The shape of \mathcal{F}_A depends on the initial and final distributions but is mainly determined by the structure of the graph on which the dynamics takes place.

The Pareto front \mathcal{F}_Σ of the partial EPs can be obtained using the Pareto front \mathcal{F}_A of the partial activities in Fig. 1(e). To maintain finite timescales for the dynamics, we set an upper bound on the activity of the total system instead of the partial activities. In general, \mathcal{F}_Σ forms a convex curve (see Fig. 1(f)), reflecting the shape of \mathcal{F}_A . When the dissipation of the total system is minimized, the dissipations of the subsystems are not necessarily minimized and can potentially be further reduced. However, the tradeoff relation is not linear, and reducing the dissipation in one subsystem requires significantly increasing the dissipation in the other subsystem. If multiple

protocols minimize the activity of the total system, this trade-off relation qualitatively changes. As a result, \mathcal{F}_Σ exhibits a linear tradeoff relation with an edge of slope -1 . Thus, it is possible to exchange dissipation among the subsystems while maintaining the optimality of the total dissipation.

In Sec. V, we apply our general results to bipartite systems to determine the optimal information processing in finite time. We consider the situation where measurement is performed before feedback, as well as the situation where they are carried out simultaneously. In such information processing, there exists a tradeoff relation between the dissipation arising from measurement and that from feedback. Moreover, increasing the activity corresponds to increasing the number of steps in information processing and enables more diverse information processing. Specifically, as the activity decreases, it becomes impossible to realize Maxwell's demon while optimizing the total dissipation. Further reducing the activity makes it impossible to realize Maxwell's demon. Finally, we present a specific protocol to implement this optimal information processing using double quantum dots.

In Sec. VI, our results are applied to a multi-state system. We examine a model of *E. coli* chemotaxis and optimize the time evolution of sensory adaptation, where one steady state relaxes to another when the ligand concentration is suddenly increased. The Wasserstein distance between these states is calculated numerically, and the optimal protocol is derived. We demonstrate that the partial EP associated with methylation and demethylation can be reduced by more than 200 times compared to the autonomous situation. This highlights the cost of achieving a specific time evolution using autonomous transition rates that violate the detailed balance condition.

II. SETUP

In this section, we provide an overview of stochastic thermodynamics in discrete systems and minimization of thermodynamic costs using optimal transport theory. Throughout this paper, the operation time τ , initial distribution p_{XY}^o , and final distribution p_{XY}^f are fixed. For simplicity, we will consider bipartite systems throughout this paper. However, results that do not involve information flow are applicable to general subsystems.

A. Stochastic Thermodynamics in Discrete Systems

We introduce the dynamics of discrete systems. State transitions can be represented as a graph $G(N, E)$, where the node set is $N = \{r\}$ and the edge set is $E = \{[r, r']\}$. Here, node r represents a state, and edge $[r, r']$ represents the tran-

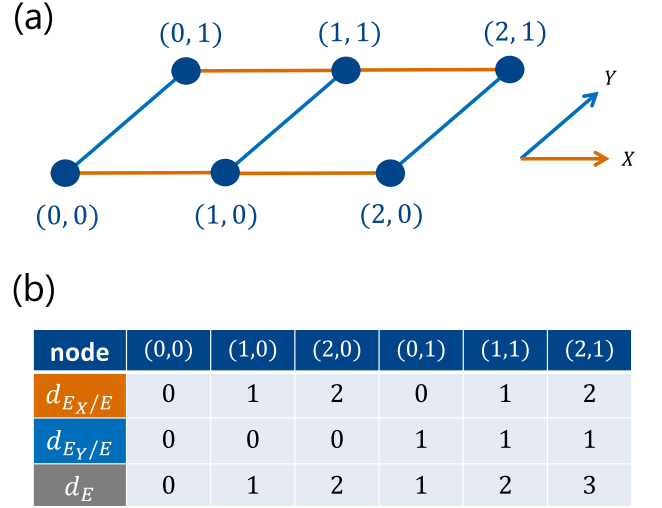


FIG. 3. (a) An example of a bipartite graph $G(N, E)$. There are no transitions where both X and Y change simultaneously. (b) The differences in the cost of transporting probability from the node $(0, 0)$ to each node in $G(N, E)$ (see Eqs. (5)(16)).

sition from state r' to r . It is assumed that if $[r, r'] \in E$, then $[r', r] \in E$. The time evolution is Markovian and can be described by the master equation using transition rates [66, 67]. The transition rates have nonzero values only on E . Furthermore, to make the dynamics consistent with thermodynamics, the transition rates are assumed to satisfy the local detailed balance condition [2].

We consider a graph $G(N, E)$ with a bipartite structure. The state r is specified by two indices of subsystems X and Y , that is, $r = (x, y)$. The transition rate from node r' to r is denoted as $R(r, r')$ and satisfies [58, 68]

$$R(r, r') = \begin{cases} R_{xx'}^y \geq 0 & (x \neq x', y = y') \\ R_{xx'}^y \geq 0 & (x = x', y \neq y') \\ 0 & (\text{otherwise}) \end{cases}. \quad (1)$$

In other words, there are no transitions where both X and Y change simultaneously (see Fig. 3(a)). The set E is expressed as the disjoint union of the sets of edges representing transitions related to X and Y , i.e., $E = E_X \sqcup E_Y$, which is defined as $E = E_X \cup E_Y$ and $E_X \cap E_Y = \emptyset$.

The probability distribution starts from the initial distribution p_{XY}^o at time $t = 0$ and evolves in time according to the master equation, reaching the final distribution p_{XY}^f at time $t = \tau (> 0)$. The master equation can be expressed as

$$\begin{aligned} d_t p_{X_t Y_t}(r) &= \sum_{r' (\neq r)} (R(r, r') p_{X_t Y_t}(r') - R(r', r) p_{X_t Y_t}(r)) \\ &= \sum_{x' (\neq x)} J_{xx'}^y + \sum_{y' (\neq y)} J_x^{yy'}. \end{aligned} \quad (2)$$

Here, $p_{X_t Y_t}(r)$ is the probability that the total system is in state $r = (x, y)$ at time t . The probability current from

state (x', y) to (x, y) is given by $J_{xx'}^y = R_{xx'}^y p_{X_t Y_t}(x', y) - R_{x'x}^y p_{X_t Y_t}(x, y)$, and the probability current from state (x, y') to (x, y) is given by $J_x^{yy'} = R_x^{yy'} p_{X_t Y_t}(x, y') - R_x^{y'y} p_{X_t Y_t}(x, y)$. These quantities may depend on time, which is not explicitly denoted for simplicity of notations.

First, we consider partial activity as a thermodynamic cost. The partial activity rates \dot{A}_X and \dot{A}_Y for subsystems X and Y are defined as [69]

$$\begin{aligned}\dot{A}_X &:= \sum_{x \neq x', y} R_{xx'}^y p_{X_t Y_t}(x', y), \\ \dot{A}_Y &:= \sum_{y \neq y', x} R_x^{yy'} p_{X_t Y_t}(x, y'),\end{aligned}\quad (3)$$

which correspond to the average number of transitions per unit time within each subsystem. These rates characterize the inverse of the relaxation times of the subsystems. The partial activities A_X and A_Y are obtained by integrating Eq. (3) over time from $t = 0$ to $t = \tau$. Increasing A_X and A_Y for a fixed τ implies operating the subsystems more quickly, thereby allowing partial activity to be considered as a cost.

Second, we consider partial EP as the other thermodynamic cost. The partial EP rates $\dot{\Sigma}_X$ and $\dot{\Sigma}_Y$ for subsystems X and Y are defined as [58]

$$\begin{aligned}\dot{\Sigma}_X &:= \sum_{x > x', y} J_{xx'}^y \ln \frac{R_{xx'}^y p_{X_t Y_t}(x', y)}{R_{x'x}^y p_{X_t Y_t}(x, y)}, \\ \dot{\Sigma}_Y &:= \sum_{y > y', x} J_x^{yy'} \ln \frac{R_x^{yy'} p_{X_t Y_t}(x, y')}{R_x^{y'y} p_{X_t Y_t}(x, y)}.\end{aligned}\quad (4)$$

These rates are nonnegative due to the inequality $(a - b) \ln(a/b) \geq 0$ for $a, b > 0$, representing the second law of thermodynamics for individual subsystems. Their magnitudes represent the irreversibility of the dynamics and the degree of energy dissipation within the subsystems. The partial EPs Σ_X and Σ_Y are obtained by integrating Eq. (4) over time.

Since $E = E_X \sqcup E_Y$, the sums of the partial activities and partial EPs equal the activity and EP of the total system, respectively: $A_{XY} = A_X + A_Y$ and $\Sigma_{XY} = \Sigma_X + \Sigma_Y$. We note that partial activities and partial EPs can be defined for any subsystem $E' \subset E$, not limited to bipartite systems [70].

B. Optimal Transport Theory and the Wasserstein Distance

Here we briefly review optimal transport theory [31, 32], in which optimal transport cost for the time evolution of probability distributions is discussed. Specifically, probability distribution q on the node set N is transformed into p by transporting probabilities through the edge set E . However, it is not necessary to transport the probability on each node injectively; it can be split and transported to multiple nodes. These transports can be represented by a transport matrix Π ,

where $\Pi(r, r') (\geq 0)$ denotes the amount transported from node r' to r . To ensure that q is completely transformed into p , the transport matrix must satisfy $\sum_r \Pi(r, r') = q(r')$ and $\sum_{r'} \Pi(r, r') = p(r)$.

To consider the optimality of transport, we define the cost associated with transport between nodes. Here, we adopt the length d_E of the shortest path on the graph as the cost function. The cost $d_E(r, r')$ is explicitly defined as

$$d_E(r, r') := \min_{\substack{P: r' \rightarrow r \\ \text{on } E}} l_E(P), \quad (5)$$

where P represents a path on E connecting node r' with r and $l_E(P)$ counts the number of edges in E traversed by P . From the definition, d_E satisfies the axioms of a distance.

The optimal transport cost under such a cost function has the properties of a distance between probability distributions and is called the (L^1) Wasserstein distance, which is defined as

$$\mathcal{W}_E(p, q) := \min_{\Pi \in \mathcal{U}(p, q)} \sum_{r, r'} d_E(r, r') \Pi(r, r'). \quad (6)$$

Here, $\mathcal{U}(p, q)$ is defined as the set of transport matrices given by $\mathcal{U}(p, q) := \{\Pi \mid \Pi(r, r') \geq 0, \sum_r \Pi(r, r') = q(r'), \sum_{r'} \Pi(r, r') = p(r)\}$, also known as the transportation polytope from q to p .

The Wasserstein distance can be bounded from below using the total variation distance $\mathcal{T}(p, q) := \sum_r |p(r) - q(r)|/2$, that is, $\mathcal{W}_E(p, q) \geq \mathcal{T}(p, q)$ holds [39]. In particular, when the graph $G(N, E)$ is fully connected, the equality is achieved. Whereas the total variation distance focuses only on the differences in the values of the probability distributions, the Wasserstein distance also takes into account the configurational differences of these distributions.

C. Review: Minimal Thermodynamic Costs of the Total System

We next review the minimization of the thermodynamic cost of the total system using optimal transport theory following Ref. [38], which plays a central role in our study. Activity and EP can be interpreted as the thermodynamic costs associated with the time evolution of the probability distribution [13, 15]. This perspective is closely related to optimal transport theory, which discusses the cost of transporting probability distributions. In fact, as we will see below, the minimum values of activity and EP can be expressed using the Wasserstein distance.

1. Minimal activity

First, we consider minimizing the activity rate in the infinitesimal time evolution $p_{X_t Y_t} \rightarrow p_{X_{t+dt} Y_{t+dt}}$. The initial

distribution $p_{X_t Y_t}$ and the final distribution $p_{X_{t+dt} Y_{t+dt}}$ are fixed. There are numerous transition rates that can realize this time evolution. Here, we optimize the transition rates to minimize the activity rate $\dot{A}_{XY} := \dot{A}_X + \dot{A}_Y$ of the total system. This minimum value can be expressed using the Wasserstein distance (6) as [38]

$$\min_{R: p_{X_t Y_t} \rightarrow p_{X_{t+dt} Y_{t+dt}}} \dot{A}_{XY} = \frac{\mathcal{W}_E(p_{X_{t+dt} Y_{t+dt}}, p_{X_t Y_t})}{dt} =: \dot{\mathcal{L}}_E. \quad (7)$$

The optimization variable R denotes the transition rates defined on E that give the time evolution of Eq. (2). We note that $\dot{\mathcal{L}}_E$ can be interpreted as the speed of time evolution measured by the Wasserstein distance.

We next consider minimizing the activity over the finite time evolution $\{p_{X_t Y_t}\}_{0 \leq t \leq \tau}$. Here, $\{p_{X_t Y_t}\}_{0 \leq t \leq \tau}$ represents a (continuous) trajectory of probability distributions, specifying the distribution at each moment. For this trajectory, the infinitesimal time procedure can be repeated at each moment, and the minimum value of the activity is given by $\mathcal{L}_E := \int_0^\tau dt \dot{\mathcal{L}}_E$. This represents the length of the trajectory measured by the Wasserstein distance.

Finally, we consider minimizing the activity for the finite-time evolution $p_{XY}^o \rightarrow p_{XY}^f$. In this case, only the initial distribution p_{XY}^o and the final distribution p_{XY}^f are fixed, and the trajectory of probability distributions during the intermediate time is also optimized. Given the fact that the Wasserstein distance satisfies the triangle inequality, the minimum value of the activity obtained when optimizing the trajectory is

$$\min_{\{R\}_{0 \leq t \leq \tau}: p_{XY}^o \rightarrow p_{XY}^f} A_{XY} = \mathcal{W}_E(p_{XY}^f, p_{XY}^o). \quad (8)$$

The optimization variable $\{R\}_{0 \leq t \leq \tau}$ denotes a protocol consisting of transition rates defined on E , which realizes the time evolution $p_{XY}^o \rightarrow p_{XY}^f$ according to Eq. (2).

The trajectory that provides the minimum value in Eq. (8) corresponds to the geodesic under the Wasserstein distance. However, this geodesic is not necessarily unique in general. One possible geodesic is the linear interpolation between the initial and final distributions, given by $p_{X_t Y_t} = (1 - t/\tau)p_{XY}^o + (t/\tau)p_{XY}^f$.

2. Minimal entropy production

First, we consider minimizing the EP rate in the infinitesimal time evolution $p_{X_t Y_t} \rightarrow p_{X_{t+dt} Y_{t+dt}}$. We optimize the transition rates that realize this time evolution to minimize the EP rate $\dot{\Sigma}_{XY} := \dot{\Sigma}_X + \dot{\Sigma}_Y$ of the total system. To keep the system's time scale finite, we impose an upper bound on the total activity rate \dot{A}_{XY} . According to Eq. (7), this upper bound must be set to at least $\dot{\mathcal{L}}_E$. In this case, the minimum

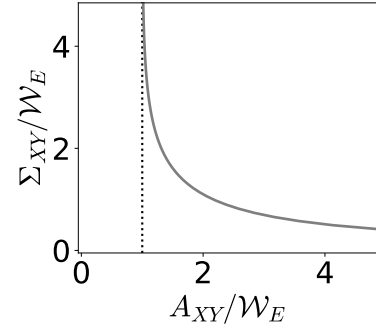


FIG. 4. The tradeoff relation between activity and EP (Eq. (10)).

value of the total EP rate is given by [38]

$$\min_{\substack{R: p_{X_t Y_t} \rightarrow p_{X_{t+dt} Y_{t+dt}} \\ A_{XY} \text{ fixed}}} \dot{\Sigma}_{XY} = 2\dot{\mathcal{L}}_E \tanh^{-1} \left(\frac{\dot{\mathcal{L}}_E}{\dot{A}_{XY}} \right). \quad (9)$$

Next, we consider minimizing the EP over the finite-time evolution $\{p_{X_t Y_t}\}_{0 \leq t \leq \tau}$. Let \mathcal{L}_E be the length of this trajectory measured by the Wasserstein distance. To keep the system's time scale finite, we impose an upper bound on the total activity A_{XY} . In this case, the minimum value of the EP is given by $2\mathcal{L}_E \tanh^{-1}(\mathcal{L}_E/A_{XY})$.

Furthermore, we optimize the trajectory to minimize the EP in the finite-time evolution $p_{XY}^o \rightarrow p_{XY}^f$. Considering that $x \tanh^{-1}(x)$ ($x > 0$) is monotonically increasing, it is clear that when optimizing the trajectory, one should select the trajectory that provides the geodesic distance $\mathcal{W}_E(p_{XY}^f, p_{XY}^o)$. Therefore, the minimum value of the EP is given by

$$\min_{\substack{\{R\}_{0 \leq t \leq \tau}: p_{XY}^o \rightarrow p_{XY}^f \\ A_{XY} \text{ fixed}}} \Sigma_{XY} = 2\mathcal{W}_E \tanh^{-1} \left(\frac{\mathcal{W}_E}{A_{XY}} \right), \quad (10)$$

where $\mathcal{W}_E = \mathcal{W}_E(p_{XY}^f, p_{XY}^o)$, and the upper bound of the activity must be chosen to satisfy $A_{XY} \geq \mathcal{W}_E(p_{XY}^f, p_{XY}^o)$. Similar to the case of minimizing the activity, the trajectory that provides the minimum EP is a geodesic in the sense of the Wasserstein distance (see the optimal protocol in Supplemental Material). However, unlike the continuous case [36], it is not necessary to maintain a constant evolution speed $\dot{\mathcal{L}}_E$.

As is clear from Eq. (10) and Fig. 4, there is a tradeoff relation between activity and EP, which can be expressed solely in terms of the thermodynamic force $F = 2 \tanh^{-1}(\mathcal{W}_E/A_{XY})$ (see Supplemental Material for details). When $F \rightarrow 0$, the transport becomes fully bidirectional, corresponding to the quasistatic limit. In this case, the dissipation asymptotically approaches zero, whereas the activity diverges. Conversely, when $F \rightarrow \infty$, the transport becomes completely unidirectional, corresponding to the strong nonequilibrium limit. In this limit, the dissipation logarithmically diverges, and the activity asymptotically approaches its minimum value \mathcal{W}_E .

3. Thermodynamic speed limit

Equality (10) can also be interpreted as a speed limit for the time evolution of the total system. Let us define the average activity rate as $\bar{A}_{XY} := A_{XY}/\tau$, which provides a scale for the inverse of the relaxation time. Furthermore, it is possible to construct a protocol that realizes Eq. (10) and satisfies $\bar{A}_{XY} = \dot{A}_{XY}$. The operation time τ must then satisfy

$$\tau \geq \tau_{XY} := \frac{\mathcal{W}_E}{\bar{A}_{XY}} \coth\left(\frac{\Sigma_{XY}}{2\mathcal{W}_E}\right). \quad (11)$$

Therefore, to achieve the desired time evolution in a shorter duration, a higher thermodynamic cost must be paid. For processes with large dissipation, where $\Sigma_{XY} \gg \mathcal{W}_E$ and $\coth(x) \simeq 1$, the activity rate \bar{A}_{XY} dominantly determines the operation time [71].

By using the inequality $\coth(x) \geq 1/x$ ($x > 0$) and $\mathcal{W}_E(p_{XY}^f, p_{XY}^o) \geq \mathcal{T}(p_{XY}^f, p_{XY}^o)$ in Eq. (11), the speed limit derived by Ref. [13] can be reproduced. However, since \mathcal{W}_E reflects the structure of the graph, Eq. (11) is tighter in general, and there exists a protocol that achieves the equality for any distributions p_{XY}^o and p_{XY}^f . This tightness becomes more pronounced as the system size increases [40].

III. MINIMAL THERMODYNAMIC COSTS OF A SINGLE SUBSYSTEM

In this section, we consider the extent to which the activity and EP of subsystems can be minimized in finite-time processes. Here, we optimize the costs of subsystems using two methods with different constraints.

First, we define partial time evolution. For simplicity, we consider minimization in the case of infinitesimal time evolution $p_{X_t Y_t} \rightarrow p_{X_{t+dt} Y_{t+dt}}$. In Eq. (2), we separate the probability flux for each subsystem and consider the partial time evolution resulting from it:

$$p_{X_{t+dt} Y_t}(r) = p_{X_t Y_t}(r) + \sum_{x'(\neq x)} J_{xx'}^y dt, \quad (12)$$

$$p_{X_t Y_{t+dt}}(r) = p_{X_t Y_t}(r) + \sum_{y'(\neq y)} J_x^{yy'} dt. \quad (13)$$

Here, $p_{X_{t+dt} Y_t}$ and $p_{X_t Y_{t+dt}}$ are joint distributions shifted by dt in time, capturing the individual time evolution of X and Y , respectively. In the following, quantities of order $o(dt)$ will be neglected. Given the transition rates of Eq. (2), the partial time evolutions (Eqs. (12)(13)) are uniquely determined. However, when only the infinitesimal time evolution $p_{X_t Y_t} \rightarrow p_{X_{t+dt} Y_{t+dt}}$ of the total system is provided, there is freedom in choosing the partial time evolution. In local optimization, a single partial time evolution is fixed, whereas in global optimization, the partial time evolution is also optimized (see Fig. 5(a)(b)).

A. Local Optimization

In this subsection, we discuss local optimization, where the transition rates on E_X are optimized to minimize the thermodynamic cost of X (see Fig. 5(a)(b)). In this approach, the partial time evolutions (see Eqs. (12)(13)) are fixed, and the optimization within each subsystem is independent. Local optimization is crucial for understanding the subsequent global optimization, and it also explains the origin of the tradeoff relation between thermodynamic costs through its procedure.

First, we consider minimization in the case of infinitesimal time evolution $p_{X_t Y_t} \rightarrow p_{X_{t+dt} Y_{t+dt}}$. The initial distribution $p_{X_t Y_t}$ and final distribution $p_{X_{t+dt} Y_{t+dt}}$ are fixed. In local optimization, the partial time evolution $p_{X_t Y_t} \rightarrow p_{X_{t+dt} Y_t}$ is also fixed, which in turn determines $p_{X_t Y_{t+dt}}$. The transitions of X occur on E_X and contribute solely to the time evolution $p_{X_t Y_t} \rightarrow p_{X_{t+dt} Y_t}$, meaning that the transitions of Y are not involved in this time evolution. Therefore, the approach of Sec. II C can be applied to the subgraph $G(N, E_X)$ and the time evolution $p_{X_t Y_t} \rightarrow p_{X_{t+dt} Y_t}$. The local minimum of the partial activity rate for X is

$$\begin{aligned} \min_{R_X: p_{X_t Y_t} \rightarrow p_{X_{t+dt} Y_t}} \dot{A}_X &= \frac{\mathcal{W}_{E_X}(p_{X_{t+dt} Y_t}, p_{X_t Y_t})}{dt} \\ &=: \dot{\mathcal{L}}_{E_X}. \end{aligned} \quad (14)$$

Here, R_X denotes the transition rates on the subset E_X of E , satisfying Eq. (12). However, if there is no path between nodes r and r' that is entirely within the edges of E_X , we define $d_{E_X}(r, r') = \infty$.

Next, we locally optimize the partial EP rate. To keep the time scale of the subsystems finite, we set an upper bound $\dot{A}_X (\geq \dot{\mathcal{L}}_{E_X})$ on the partial activity rate. Similar to the case of the partial activity, we can apply the approach from Sec. II C. As a result, the local minimum of the partial EP rate for X is

$$\min_{\substack{R_X: p_{X_t Y_t} \rightarrow p_{X_{t+dt} Y_t} \\ \dot{A}_X \text{ fixed}}} \dot{\Sigma}_X = 2\dot{\mathcal{L}}_{E_X} \tanh^{-1}\left(\frac{\dot{\mathcal{L}}_{E_X}}{\dot{A}_X}\right). \quad (15)$$

Extending to the finite time evolution $p_{XY}^o \rightarrow p_{XY}^f$ is straightforward. In this case, the trajectory of the probability distribution $\{p_{X_t Y_t}\}_{0 \leq t \leq \tau}$ is fixed. Furthermore, by fixing the partial time evolution at each moment, local optimization becomes possible. The minimum partial activity of X is given by $\mathcal{L}_{E_X} := \int_0^\tau dt \dot{\mathcal{L}}_{E_X}$. Moreover, by fixing the upper bound of the partial activity $\dot{A}_X (\geq \mathcal{L}_{E_X})$, the minimum partial EP is given by $2\mathcal{L}_{E_X} \tanh^{-1}(\mathcal{L}_{E_X}/\dot{A}_X)$.

In local optimization, the partial time evolutions $p_{X_{t+dt} Y_t}$ and $p_{X_t Y_{t+dt}}$ are fixed. Since information flow is expressed using $p_{X_{t+dt} Y_t}$ and $p_{X_t Y_{t+dt}}$, this can be considered as fixing the information flow (see Eqs. (33)(34)).

The optimization given in Eqs. (14)(15) applies similarly to the subsystem Y . Since R_X and R_Y can be optimized independently, the local minima of the thermodynamic costs for

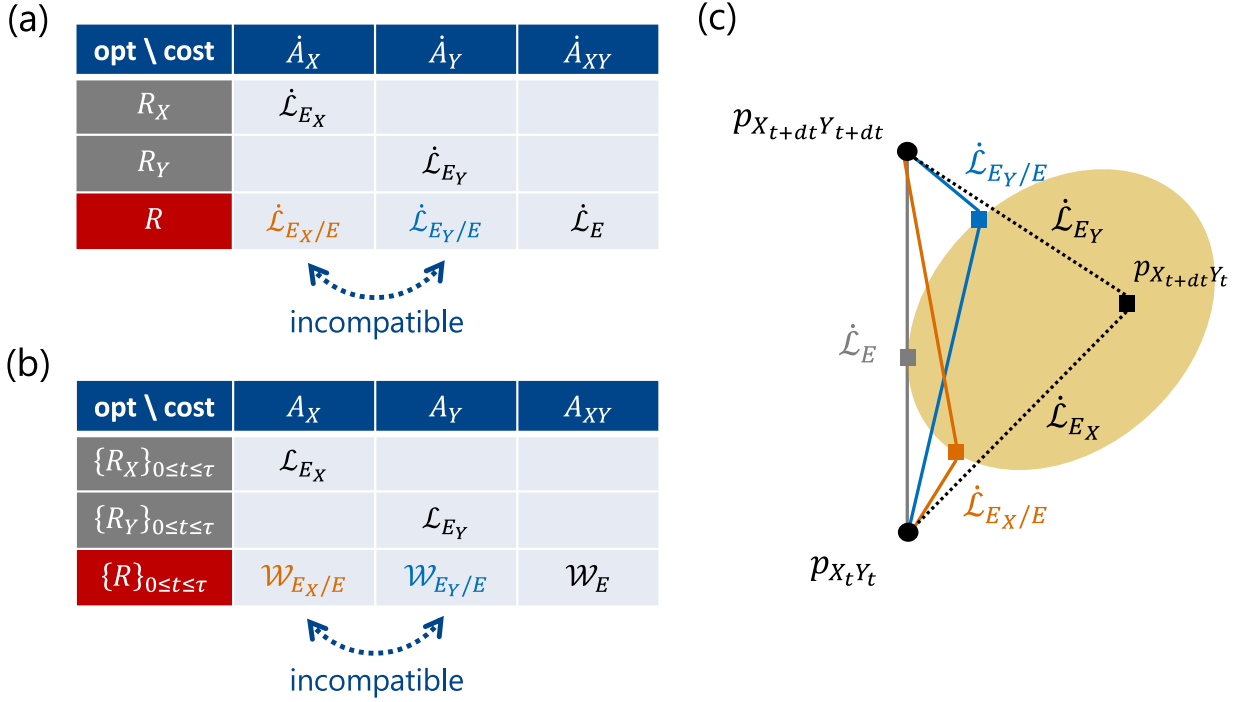


FIG. 5. (a)(b) Differences in the optimization target and method for infinitesimal time evolution $p_{X_t Y_t} \rightarrow p_{X_{t+dt} Y_{t+dt}}$ and finite time evolution $p_{X_t Y_t}^o \rightarrow p_{X_t Y_t}^f$. The gray cells represent local optimization, optimizing only the transition rates related to subsystem transitions while keeping the partial time evolution $p_{X_{t+dt} Y_{t+dt}}$ fixed. The red cells represent global optimization, where the entire transition rates are optimized. In this case, the partial time evolution is also optimized. In the local optimization for finite time evolution, the overall time evolution $\{p_{X_t Y_t}\}_{0 \leq t \leq \tau}$ is not modified. Therefore, the minimum is not \mathcal{W} , which depends only on the initial and final distributions, but \mathcal{L} , which depends on the trajectory of the distribution. The same applies when minimizing the partial EP (rate). (c) Differences in partial time evolution for infinitesimal time evolution $p_{X_t Y_t} \rightarrow p_{X_{t+dt} Y_{t+dt}}$. This corresponds to the infinitesimal time version of the central schematic diagram in Fig. 1. The shaded area schematically represents the range of $p_{X_{t+dt} Y_{t+dt}}$, specifically the range where $\dot{\mathcal{L}}_{E_X} < \infty$ and $\dot{\mathcal{L}}_{E_Y} < \infty$. The gray line represents the optimal transport of the total system (Eq. (7)), corresponding to the geodesic under the Wasserstein distance. For any $p_{X_{t+dt} Y_{t+dt}}$, the inequality $\dot{\mathcal{L}}_{E_X} + \dot{\mathcal{L}}_{E_Y} \geq \dot{\mathcal{L}}_E$ holds (see Supplemental Material for details).

the subsystems can be achieved simultaneously. However, for the overall time evolution $p_{X_t Y_t} \rightarrow p_{X_{t+dt} Y_{t+dt}}$ to be possible, the time evolution $p_{X_t Y_t} \rightarrow p_{X_{t+dt} Y_{t+dt}}$ must be realized solely by R_X , and the time evolution $p_{X_{t+dt} Y_{t+dt}} \rightarrow p_{X_t Y_t}$ (which is the same as $p_{X_t Y_t} \rightarrow p_{X_{t+dt} Y_{t+dt}}$) must be realized solely by R_Y . In other words, $p_{X_{t+dt} Y_{t+dt}}$ (or $p_{X_t Y_t}$) must be chosen such that $\dot{\mathcal{L}}_{E_X} < \infty$ and $\dot{\mathcal{L}}_{E_Y} < \infty$ are satisfied (see Fig. 5(c)).

The transition rates that achieve the minimum value in Eq. (14) can be expressed using the optimal transport matrix concerning d_{E_X} within $\mathcal{U}(p_{X_{t+dt} Y_{t+dt}}, p_{X_t Y_t})$. Similarly, the transition rates R_X that achieve the minimum value in Eq. (15) can be expressed using this optimal transport matrix and the thermodynamic force on E_X , $F_X = 2 \tanh^{-1}(\dot{\mathcal{L}}_{E_X}/\dot{A}_X)$ (see Supplemental Material for details). In the case of finite time evolution, F_X needs to be kept constant at each time step. From the transport perspective, the thermodynamic force F_X characterizes the unidirectionality of transport on the edges E_X . There is a tradeoff relation between the activity rate and the EP rate for X , which can be

represented solely by the parameter F_X .

B. Global Optimization

In this subsection, we discuss global optimization, where the overall transition rates are optimized to minimize the thermodynamic cost of X . In this approach, the previously fixed partial time evolutions are also optimized. This allows for further minimization of the costs of subsystem X beyond what local optimization (Eqs. (14)(15)) can achieve. To this end, we introduce a generalization of the Wasserstein distance. Unlike local optimization, this approach does not treat the optimization within each subsystem independently. Physically, this can be interpreted as optimizing the cost of X under the condition that X and Y can interact in any manner. The same procedure can be applied to optimize Y as well, while we focus only on X in the following.

1. Minimal partial activity

First, consider minimizing the partial activity rate in the case of infinitesimal time evolution $p_{X_t Y_t} \rightarrow p_{X_{t+dt} Y_{t+dt}}$. The initial distribution $p_{X_t Y_t}$ and final distribution $p_{X_{t+dt} Y_{t+dt}}$ are fixed. In Sec. III A, we performed local optimization by fixing the partial time evolution $p_{X_t Y_t} \rightarrow p_{X_{t+dt} Y_t}$. In this subsection, we perform global optimization by also allowing $p_{X_{t+dt} Y_t}$ to vary. In this optimization, under the condition that the entire transition rates realize the time evolution $p_{X_t Y_t} \rightarrow p_{X_{t+dt} Y_{t+dt}}$, we aim to minimize the transitions carried by the X component of the transition rates as much as possible. Specifically, we select $p_{X_{t+dt} Y_t}$ such that $\dot{\mathcal{L}}_{E_Y} < \infty$ and $\dot{\mathcal{L}}_{E_X}$ is minimized.

To find the partial time evolution that minimizes the transitions on E_X , we consider the cost function $d_{E_X/E}$ defined as

$$d_{E_X/E}(r, r') := \min_{\substack{P: r' \rightarrow r \\ \text{on } E}} l_{E_X}(P). \quad (16)$$

Although the cost function d_E (Eq. (5)) counts all transports on E , $d_{E_X/E}$ counts only the transports on E_X (see Fig. 3(b)). The optimal transport cost concerning this cost function $d_{E_X/E}$ is expressed as

$$\mathcal{W}_{E_X/E}(p, q) := \min_{\Pi \in \mathcal{U}(p, q)} \sum_{r, r'} d_{E_X/E}(r, r') \Pi(r, r'), \quad (17)$$

which is regarded as a generalized Wasserstein distance as explained below. The quantity $\mathcal{W}_{E_X/E}(p, q)$ represents the minimum transport cost related to E_X for transporting the probability distribution q to p . Intuitively, in the optimal transport matrix concerning $d_{E_X/E}$, all transport that can be performed on E_Y is carried out on E_Y .

Similar to \mathcal{W}_E and \mathcal{W}_{E_X} , $\mathcal{W}_{E_X/E}$ satisfies the properties of symmetry and the triangle inequality, that is, $\mathcal{W}_{E_X/E}(p, q) = \mathcal{W}_{E_X/E}(q, p)$ and $\mathcal{W}_{E_X/E}(p, r) \leq \mathcal{W}_{E_X/E}(p, q) + \mathcal{W}_{E_X/E}(q, r)$. The triangle inequality allows this optimization to be extended to the time-integrated case. However, since $\mathcal{W}_{E_X/E}(p, q) = 0$ when the transport can be performed solely on E_Y , $\mathcal{W}_{E_X/E}$ is a pseudo-distance rather than a true distance. Here, we refer to $\mathcal{W}_{E_X/E}$ as the Wasserstein pseudo-distance. The same applies to $\mathcal{W}_{E_Y/E}$.

Using this Wasserstein pseudo-distance, the minimum partial activity rate of X for the infinitesimal time evolution $p_{X_t Y_t} \rightarrow p_{X_{t+dt} Y_{t+dt}}$ can be expressed as:

$$\begin{aligned} \min_{R: p_{X_t Y_t} \rightarrow p_{X_{t+dt} Y_{t+dt}}} \dot{A}_X &= \frac{\mathcal{W}_{E_X/E}(p_{X_{t+dt} Y_{t+dt}}, p_{X_t Y_t})}{dt} \\ &=: \dot{\mathcal{L}}_{E_X/E}. \end{aligned} \quad (18)$$

By using Eq. (17), we perform both the local optimization and the optimization of partial time evolution. The condition $\Pi \in \mathcal{U}(p_{X_{t+dt} Y_{t+dt}}, p_{X_t Y_t})$ during the optimization ensures

that $\dot{\mathcal{L}}_{E_X} < \infty$ and $\dot{\mathcal{L}}_{E_Y} < \infty$ are satisfied. By using the cost function $d_{E_X/E}$, we minimize the partial activity rate of X . In local optimization (Eq. (14)), we optimized the X component of the transition rates, R_X . By contrast, in global optimization (Eq. (18)), we optimize the entire transition rates, R . The proof of Eq. (18) is provided in Supplemental Material.

Next, we consider minimizing the partial activity for the finite time evolution $p_{X_Y}^o \rightarrow p_{X_Y}^f$. Only the initial distribution $p_{X_Y}^o$ and the final distribution $p_{X_Y}^f$ are fixed, and the trajectory of the probability distributions corresponding to the intermediate time evolution is also optimized. Since $\mathcal{W}_{E_X/E}$ satisfies the triangle inequality, similar to Eq. (8), the minimum partial activity is given by:

$$\min_{\{R\}_{0 \leq t \leq \tau}: p_{X_Y}^o \rightarrow p_{X_Y}^f} A_X = \mathcal{W}_{E_X/E}(p_{X_Y}^f, p_{X_Y}^o). \quad (19)$$

In this case, the trajectory forms a geodesic under the Wasserstein pseudo-distance, which generally differs from the geodesic under the standard Wasserstein distance. However, the linear interpolation between the initial and final distributions $p_{X_t Y_t} = (1 - t/\tau)p_{X_Y}^o + (t/\tau)p_{X_Y}^f$ can be used as a common geodesic.

The optimization in Eq. (18) can also be performed similarly for the subsystem Y . However, it should be noted that, in general, the transition rates R (and the resulting partial time evolutions $p_{X_{t+dt} Y_t}$ and $p_{X_t Y_{t+dt}}$) that minimize the partial activity rates for X and Y may be different. This difference arises because the optimal transport matrices concerning $d_{E_X/E}$ and $d_{E_Y/E}$ within $\mathcal{U}(p_{X_{t+dt} Y_{t+dt}}, p_{X_t Y_t})$ are different. Therefore, in general, it is not possible to simultaneously achieve the globally minimal partial activity rates $\dot{\mathcal{L}}_{E_X/E}$ and $\dot{\mathcal{L}}_{E_Y/E}$ for both X and Y (see Fig. 5(c)). This implies a trade-off relation where reducing the activity rate of one subsystem will increase the activity rate of the other subsystem. Naturally, the global minimum of the total activity rate $\dot{\mathcal{L}}_E$ is given by the optimal transport of the total system. The same applies to the time-integrated case. The bounds of the tradeoff relation in partial activities will be discussed in the next section.

The transition rates that achieve Eq. (18) can be constructed similarly to those in Eq. (7). However, when converting the optimal transport matrix into transition rates, it is necessary to select paths that minimize the use of edges in E_X as much as possible (see Supplemental Material for details).

2. Minimal partial entropy production

First, we consider minimizing the partial EP rate in the overall infinitesimal time evolution $p_{X_t Y_t} \rightarrow p_{X_{t+dt} Y_{t+dt}}$. To keep the timescale of the subsystem X finite, we set an upper bound $\dot{A}_X (\geq \dot{\mathcal{L}}_{E_X/E})$ on the activity rate of X . In the global optimization of the partial EP rate, in addition to the local optimization in the previous section (Eq. (15)), the partial

time evolution is also optimized. This optimal time evolution is determined by the minimization of the partial activity rate (Eq. (18)). Therefore, the global minimum partial EP for X is given by

$$\min_{\substack{R: p_{X_t Y_t} \rightarrow p_{X_{t+dt} Y_{t+dt}} \\ \bar{A}_X \text{ fixed}}} \dot{\Sigma}_X = 2\dot{\mathcal{L}}_{E_X/E} \tanh^{-1} \left(\frac{\dot{\mathcal{L}}_{E_X/E}}{\bar{A}_X} \right). \quad (20)$$

Next, we minimize the partial EP for finite time evolution $p_{XY}^o \rightarrow p_{XY}^f$. To keep the timescale of the subsystem X finite, we set an upper bound $A_X (\geq \mathcal{W}_{E_X/E})$ on the partial activity. As in the case of the total system (Eq. (10)), we optimize the trajectory of the time evolution. In global optimization, we further optimize the partial time evolution within this trajectory. This optimal time evolution is determined by the minimization of the partial activity (Eq. (19)). Therefore, the global minimum of the partial EP for finite time evolution is given by

$$\min_{\substack{\{R\}_{0 \leq t \leq \tau: p_{XY}^o \rightarrow p_{XY}^f} \\ \bar{A}_X \text{ fixed}}} \Sigma_X = 2\mathcal{W}_{E_X/E} \tanh^{-1} \left(\frac{\mathcal{W}_{E_X/E}}{\bar{A}_X} \right). \quad (21)$$

The optimization in Eqs. (20)(21) can also be performed similarly for the subsystem Y . However, similarly to the partial activity, it is in general not possible to simultaneously achieve the global minimum of the partial EP for both X and Y . This is because the optimality of the partial evolution, which needs to be specified to calculate thermodynamic costs of X and Y , is different for X and Y (see Fig. 5(c)). Therefore, there exists a tradeoff relation where reducing the EP of one subsystem increases the EP of the other subsystem.

Similar to the case of Eq. (15), the transition rates R that achieve the minimum value in Eq. (20) can be constructed. However, since the thermodynamic cost of Y is not the optimization target, the thermodynamic force F_Y on E_Y can be chosen arbitrarily. The same applies to the time-integrated case. We note that the entropy productions of subsystems can be lower-bounded through marginalization (see Supplemental Material for details).

3. Thermodynamic speed limit

Equality (21) and its counterpart for Y can also be interpreted as the speed limits for the time evolution. Let us define the average partial activity rates as $\bar{A}_X := A_X/\tau$ and $\bar{A}_Y := A_Y/\tau$. This gives the scale of the inverse of the relaxation time for each subsystem. Combined with Eq. (11), the

operation time τ satisfies the following speed limit:

$$\tau \geq \max\{\tau_X, \tau_Y, \tau_{XY}\}, \quad (22)$$

$$\tau_X := \frac{\mathcal{W}_{E_X/E}}{\bar{A}_X} \coth \left(\frac{\Sigma_X}{2\mathcal{W}_{E_X/E}} \right), \quad (23)$$

$$\tau_Y := \frac{\mathcal{W}_{E_Y/E}}{\bar{A}_Y} \coth \left(\frac{\Sigma_Y}{2\mathcal{W}_{E_Y/E}} \right). \quad (24)$$

These speed limits can be interpreted as follows. We want to evolve the system from the initial distribution p_{XY}^o to the final distribution p_{XY}^f over the graph $G(N, E = E_X \sqcup E_Y)$ by manipulating the transition rates. During the evolution, we are allowed to dissipate in each subsystem up to Σ_X and Σ_Y , respectively. The operation speed of each subsystem is finite, and the partial activity rates cannot exceed \bar{A}_X and \bar{A}_Y , respectively. These parameters can be set arbitrarily. The speed limit (22) indicates that we need an operation time of at least $\max\{\tau_X, \tau_Y, \tau_{XY}\}$. Therefore, to achieve the desired time evolution in a shorter period, it is necessary to increase the dissipation for both X and Y .

4. Several remarks

The protocol that provides the global minimum of the partial activity and partial EP can be expressed using the optimal transport matrix concerning $d_{E_X/E}$ or $d_{E_Y/E}$ within $\mathcal{U}(p_{XY}^f, p_{XY}^o)$. However, in general, such (L^1) optimal transport matrices are not uniquely determined [38, 72]. This is because there may be multiple paths on $G(N, E)$ that give the same optimal transport cost. Moreover, even if one selects an optimal path, there is freedom in how to perform the transport within that path. These generate different trajectories that yield distinct geodesics. For any trajectory, the partial activity and partial EP remain unchanged if the same thermodynamic force is applied, but the time-integrated information flow may vary. This point is discussed in Sec. V. Furthermore, there is also freedom in determining the time dependency of the evolution speeds $\dot{\mathcal{L}}_{E_X}$ and $\dot{\mathcal{L}}_{E_Y}$. Partial activity, partial EP, and the time-integrated information flow do not depend on this speed. In contrast, for continuous systems, this speed needs to be constant to minimize the dissipation [36].

IV. TRADEOFF RELATIONS IN THE THERMODYNAMIC COSTS OF SUBSYSTEMS

In this section, we consider the framework to identify the tradeoff relation between the thermodynamic costs of X and Y in finite-time processes. Hereafter, when the initial and final distributions are clear from the context, we will omit these variables of the Wasserstein distance.

A. Pareto Front

As a tool to express the tradeoff relations between conflicting cost functions, we adopt the Pareto front [73, 74]. Figure 6(a) represents a general schematics of the Pareto front. The feasible region $K_C (\neq \emptyset)$ consists of all pairs of feasible cost functions $C = (C_X, C_Y)$. The Pareto front \mathcal{F}_C is the set of all optimal pairs within K_C (see the precise definition in Supplemental Material). In other words, the Pareto front corresponds to finding the minimum C_X for a fixed value of C_Y . We note that the Pareto front has been applied in thermodynamics to characterize the tradeoff relations in thermodynamic machines, such as those between power and efficiency, or dissipation and precision [75–77]. We here introduce the concept of the Pareto front for thermodynamic costs of subsystems C and provide a general method for constructing it.

The explicit method to construct the Pareto front \mathcal{F}_C is explained as follows [78]. Take $0 \leq s \leq 1$ and perform the following procedure (see also Fig. 6(a)): First, among all protocols $\{R\}_{0 \leq t \leq \tau}$ that realize the time evolution $p_{XY}^o \rightarrow p_{XY}^f$, minimize the weighted cost function $sC_X + (1-s)C_Y$, i.e., solve

$$\min_{\{R\}_{0 \leq t \leq \tau}: p_{XY}^o \rightarrow p_{XY}^f} [sC_X + (1-s)C_Y]. \quad (25)$$

Then, plot all points (C_X, C_Y) corresponding to the protocols that give the minimum value. After sweeping s over the range $0 \leq s \leq 1$, the set of optimal points obtained by this method forms the Pareto front if K_C is a convex set [78].

B. Pareto Front of the Partial Activities

First, we consider the Pareto front \mathcal{F}_A of partial activities A_X, A_Y . It can be shown that the feasible region for partial activity, K_A , is convex (see Supplemental Material for proof). Furthermore, such optimization can be reduced to optimal transport theory in the case of partial activity, which will be discussed in the following. With $C = A$ and $s = 1$, Eq. (25) corresponds to the global minimization of the activity of X , and its minimum value is given by Eq. (19). To find this minimum value, we introduced the cost function $d_{E_X/E}$ of the optimal transport problem. Similarly, by designing the cost function appropriately, the minimum value of Eq. (25) for other values of s can also be expressed using the Wasserstein distance.

To find the minimum value of Eq. (25), we introduce the following cost function. Define $d_{E_X:E_Y}^s$ ($0 \leq s \leq 1$) as

$$d_{E_X:E_Y}^s(r, r') := \min_{\substack{P: r' \rightarrow r \\ \text{on } E}} [s l_{E_X}(P) + (1-s) l_{E_Y}(P)]. \quad (26)$$

The optimal transport cost regarding this cost function is then

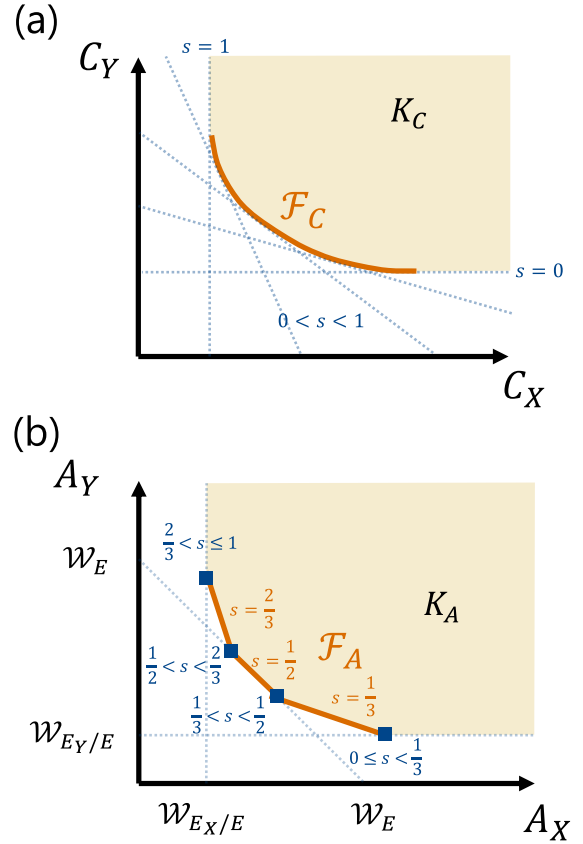


FIG. 6. (a) A schematic diagram of the Pareto front \mathcal{F}_C for incompatible cost functions C_X and C_Y . The yellow-shaded area represents the feasible region K_C for (C_X, C_Y) . To obtain the Pareto front \mathcal{F}_C , solve Eq. (25) for $0 \leq s \leq 1$. Specifically, for each s , find the tangent line to K_C with a slope of $-s/(1-s)$ (blue dashed line in the figure). (b) A typical example of the Pareto front \mathcal{F}_A of partial activities in the finite-time evolution $p_{XY}^o \rightarrow p_{XY}^f$. This figure illustrates that \mathcal{F}_A consists of vertices (blue squares) and edges (orange lines). For instance, the vertex for $1/2 < s < 2/3$ indicates that $sA_X + (1-s)A_Y$ is minimized at this point for values of s in this range. Conversely, the edge for $s = 2/3$ indicates that $sA_X + (1-s)A_Y$ is minimized along this edge for this value of s .

given by

$$\mathcal{W}_{E_X:E_Y}^s(p, q) := \min_{\Pi \in \mathcal{U}(p, q)} \sum_{r, r'} d_{E_X:E_Y}^s(r, r') \Pi(r, r'). \quad (27)$$

Although $\mathcal{W}_{E_X/E}$ represents the minimization of the transport cost related to E_X , $\mathcal{W}_{E_X:E_Y}^s$ represents the minimization of a convex combination of the transport costs for E_X and E_Y . Similar to $\mathcal{W}_{E_X/E}$, $\mathcal{W}_{E_X:E_Y}^s$ satisfies symmetry and the triangle inequality. Moreover, for $0 < s < 1$, non-degeneracy holds, making $\mathcal{W}_{E_X:E_Y}^s$ a distance.

Following a similar argument as in Eq. (19), the minimum value of Eq. (25) for $C = A$ is given by $\mathcal{W}_{E_X:E_Y}^s(p_{XY}^o, p_{XY}^f)$ (see Supplemental Material for proof). In general, the optimal transport problem (27) is a linear programming problem, hence this minimum value can be efficiently determined. By

plotting the optimal pairs (A_X, A_Y) based on Eq. (25), we can obtain the Pareto front \mathcal{F}_A of partial activities. However, when converting the optimal transport matrix to have values only on E , it is necessary to select the path that gives the cost function $d_{E_X:E_Y}^s$ (see Supplemental Material for details).

In general, \mathcal{F}_A forms a convex polyline consisting of a finite number of vertices and edges (see Fig. 6(b)). Each vertex (blue square) indicates that within the corresponding range of s , the pair (A_X, A_Y) that minimizes $sA_X + (1-s)A_Y$ remains the same. Specifically, the vertices for $s = 1$ and $s = 0$ give the minimum partial activities $\mathcal{W}_{E_X/E}(p_{XY}^f, p_{XY}^o)$ and $\mathcal{W}_{E_Y/E}(p_{XY}^f, p_{XY}^o)$, respectively. On the other hand, each edge (orange line segment) indicates that for a specific value of s , there are multiple pairs (A_X, A_Y) that minimize $sA_X + (1-s)A_Y$, distributed linearly. As a result, \mathcal{F}_A has an edge with a slope of $-s/(1-s)$, showing a singular tradeoff behavior. Remember that to realize time evolution within a finite operation time τ , the system needs to be controlled at a certain minimum average speed. On the edges of \mathcal{F}_A , this required operational speed can be adjusted between subsystems. In particular, the edge with a slope of -1 corresponding to $s = 1/2$ represents the minimum total activity. In this case, Eq. (25) reduces to the minimization of half the total activity of the system (see Eq. (8)). This behavior can be derived from the general theory of linear programming (see Supplemental Material for details).

The Pareto front \mathcal{F}_A of partial activities depends on both the initial and final distributions, but its shape is significantly influenced by the structure of the graph $G(N, E)$. This will be illustrated with a simple example in Sec. IV D.

C. Pareto Front of the Partial EPs

We next consider the Pareto front \mathcal{F}_Σ of partial EPs Σ_X, Σ_Y . To maintain a finite timescale for the system, we set an upper bound on the total activity, $A_{XY}(\geq \mathcal{W}_{XY})$. In the context of information processing, this can be seen as imposing a limit on the number of processing steps. We can obtain \mathcal{F}_Σ by solving Eq. (25) for $C = \Sigma$ under this activity constraint. In this problem, it is necessary to consider the compatibility of the partial EPs for X and Y . This can be achieved by performing local optimization of the partial EPs (see Sec. III A) in each subsystem while ensuring that the activity bound is satisfied:

$$\begin{cases} \Sigma_X = \mathcal{L}_{E_X} F_X \\ \Sigma_Y = \mathcal{L}_{E_Y} F_Y \\ A_{XY} = \mathcal{L}_{E_X} \coth(F_X/2) + \mathcal{L}_{E_Y} \coth(F_Y/2) \end{cases}. \quad (28)$$

Here, \mathcal{L}_{E_X} and \mathcal{L}_{E_Y} are the local minima of the partial activities when the trajectory of the time evolution $\{p_{X_t Y_t}\}_{0 \leq t \leq \tau}$ and the partial time evolution $\{p_{X_t + dt Y_t}\}_{0 \leq t \leq \tau}$ are fixed. On

the other hand, F_X and F_Y (≥ 0) are the thermodynamic forces when the partial EPs are locally minimized. In this minimization, the partial activities are given by $\mathcal{L}_{E_X} \coth(F_X/2)$ and $\mathcal{L}_{E_Y} \coth(F_Y/2)$, with the thermodynamic forces set to satisfy the activity constraints (see Eq. (28)).

To solve Eq. (25), the remaining task is to optimize the time evolutions (\mathcal{L}_{E_X} and \mathcal{L}_{E_Y}) and the thermodynamic forces (F_X and F_Y). However, for \mathcal{L}_{E_X} and \mathcal{L}_{E_Y} , we only need to consider those on the Pareto front \mathcal{F}_A of partial activities. This is because, for \mathcal{L}_{E_X} and \mathcal{L}_{E_Y} not on \mathcal{F}_A , either Σ_X or Σ_Y will become larger (see Eqs. (25)(28)). In general, it is not easy to analytically determine the time evolution and thermodynamic forces that minimize Eq. (25). Nevertheless, we can obtain \mathcal{F}_Σ by sweeping the parameters as shown in Fig. 7. In Fig. 7(a), the gray polyline represents \mathcal{F}_A , and the blue square is one of its vertices. For the time evolution corresponding to this vertex, the partial EPs are plotted by varying F_X and F_Y in Eq. (28), shown as the blue line in Fig. 7(b). The corresponding partial activities are represented by the blue line in Fig. 7(a), and they satisfy the activity bound A_{XY} . By performing this procedure for all time evolutions on \mathcal{F}_A , we can obtain \mathcal{F}_Σ as shown in Fig. 7(c).

1. Special cases without parameter sweep

In the following cases, Eq. (25) can be solved without sweeping the parameters of time evolution and thermodynamic forces.

When $s = 1/2$, for any $A_{XY}(\geq \mathcal{W}_E)$, the optimal values of \mathcal{L}_{E_X} , \mathcal{L}_{E_Y} , F_X , and F_Y can be determined as follows. When $s = 1/2$, Eq. (25) reduces to minimizing (half) the EP of the total system (see Eq. (10)). First, by fixing \mathcal{L}_{E_X} and \mathcal{L}_{E_Y} and optimizing F_X and F_Y , we obtain $F_X = F_Y$. At this point, the partial activity satisfies the relation $A_X/\mathcal{L}_{E_X} = A_Y/\mathcal{L}_{E_Y}$. Then, optimizing the partial time evolution selects those that satisfy $\mathcal{L}_{E_X} + \mathcal{L}_{E_Y} = \mathcal{W}_E$. Using Fig. 7, we can illustrate the above optimization. The blue square in Fig. 7(a) represents one of the time evolutions $(\mathcal{L}_{E_X}, \mathcal{L}_{E_Y})$ that yields \mathcal{W}_E . The blue curve in Fig. 7(b) depicts the optimization of thermodynamic forces for this time evolution. The total dissipation is minimized when $F_X = F_Y$, and this curve is tangent to the black dotted line. The partial activity at this point satisfies both the orange dotted line $A_X/\mathcal{L}_{E_X} = A_Y/\mathcal{L}_{E_Y}$ and the black dotted line $A_X + A_Y = A_{XY}$ simultaneously. It should be noted that the time evolution that yields \mathcal{W}_E is not necessarily unique. When \mathcal{F}_A has an edge with a slope of -1 as in Fig. 7(a), minimum dissipation can be achieved with different time evolutions, so \mathcal{F}_Σ also has an edge with the same slope, as shown in Fig. 7(c).

Near equilibrium ($A_{XY} \gg \mathcal{W}_E$), the optimization of Eq. (25) can be performed on Eq. (28). This is equivalent

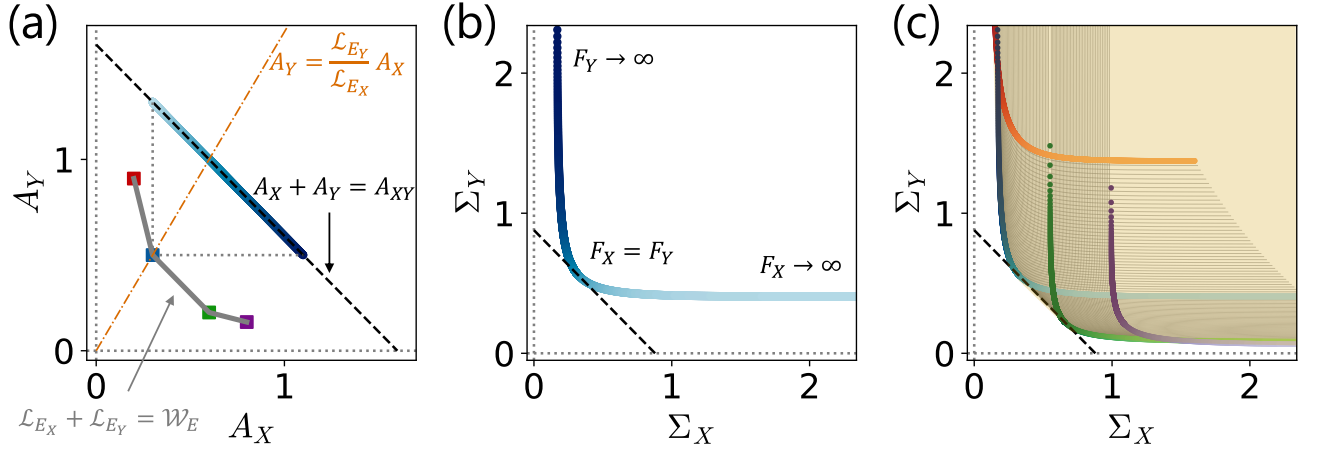


FIG. 7. (a) An illustrative example of the Pareto front \mathcal{F}_A of partial activities. \mathcal{F}_A consists of square vertices and gray edges. The vertices, ordered by increasing A_X , are $(0.2, 0.9)$, $(0.3, 0.5)$, $(0.6, 0.2)$, $(0.8, 0.15)$. (b) For the time evolution corresponding to the blue square in (a), Eq. (28) is plotted. The partial activities realized for these EPs correspond to the blue line in (a). The black dashed line indicates the minimum total EP. When the total EP is minimized, $\mathcal{L}_{E_X} + \mathcal{L}_{E_Y} = \mathcal{W}_E$, $A_X + A_Y = A_{XY}$, and $A_Y = (\mathcal{L}_{E_Y}/\mathcal{L}_{E_X})A_X$ are satisfied. The partial activity takes the value at the intersection of the black and orange dashed lines in (a). (c) The corresponding Pareto front \mathcal{F}_Σ of partial EPs. We can obtain \mathcal{F}_Σ by plotting Eq. (28) for all partial time evolutions $(\mathcal{L}_{E_X}, \mathcal{L}_{E_Y})$ that constitute \mathcal{F}_A in (a). Here, $\mathcal{W}_E = 0.8$ and $A_{XY} = 1.6$.

to minimizing the following function:

$$\begin{aligned} & s\mathcal{L}_{E_X}F_X + (1-s)\mathcal{L}_{E_Y}F_Y \\ & + \lambda(\mathcal{L}_{E_X}\coth(F_X/2) - \mathcal{L}_{E_Y}\coth(F_Y/2) - A_{XY}) \\ & \simeq s\mathcal{L}_{E_X}F_X + (1-s)\mathcal{L}_{E_Y}F_Y \\ & + \lambda\left(\frac{2\mathcal{L}_{E_X}}{F_X} + \frac{2\mathcal{L}_{E_Y}}{F_Y} - A_{XY}\right), \end{aligned} \quad (29)$$

where $\lambda(\geq 0)$ is the Lagrange multiplier. Here, near equilibrium, assuming the optimized thermodynamic forces are $F_X \simeq 0$ and $F_Y \simeq 0$, we approximate $\coth(F_X/2) \simeq 2/F_X$ and $\coth(F_Y/2) \simeq 2/F_Y$. Thus, λ becomes $\lambda = 2((\sqrt{s}\mathcal{L}_{E_X} + \sqrt{1-s}\mathcal{L}_{E_Y})/A_{XY})^2$, and the convex combination of the partial EPs after optimizing the thermodynamic forces is given by

$$s\Sigma_X + (1-s)\Sigma_Y \simeq \frac{2(\sqrt{s}\mathcal{L}_{E_X} + \sqrt{1-s}\mathcal{L}_{E_Y})^2}{A_{XY}}. \quad (30)$$

Therefore, to optimize the partial time evolutions \mathcal{L}_{E_X} and \mathcal{L}_{E_Y} , one should minimize $\sqrt{s}\mathcal{L}_{E_X} + \sqrt{1-s}\mathcal{L}_{E_Y}$. This is equivalent to the optimization problem of Eq. (25) with the coefficient s replaced by $\sqrt{s}/(\sqrt{s} + \sqrt{1-s})$. Hence, there is no need to sweep the parameter to find \mathcal{F}_Σ . Furthermore, when \mathcal{F}_A has an edge corresponding to the coefficient $\sqrt{s}/(\sqrt{s} + \sqrt{1-s})$, \mathcal{F}_Σ also has an edge corresponding to the coefficient s (i.e., the slope is squared).

2. Several remarks

When $s = 1$, Eq. (25) is analogous to the global minimization of the EP of X (Eq. (21)), but it is A_{XY} that is fixed,

not A_X . Thus, the time required for the transitions of Y must also be considered. For optimizing the thermodynamic forces, setting $F_Y \rightarrow \infty$ results in $F_X = 2\tanh^{-1}(\mathcal{L}_{E_X}/(A_{XY} - \mathcal{L}_{E_Y}))$. However, the optimization of the partial time evolutions \mathcal{L}_{E_X} and \mathcal{L}_{E_Y} is nontrivial and depends on the shape of \mathcal{F}_A .

In this section, when determining the Pareto front of partial EPs, an upper bound $A_{XY}(\geq \mathcal{W}_E(p_{XY}^f, p_{XY}^o))$ was set for the total activity. The quasistatic limit is obtained by taking $A_{XY} \rightarrow \infty$. This constraint was imposed to maintain finite time scales for both subsystems, but there are other possible methods for setting such constraints. For example, one could fix the upper bounds of the partial activities A_X and A_Y as in Eq. (21). It is necessary to examine whether these upper bounds can be simultaneously satisfied. In this case, there still exists the tradeoff relation between Σ_X and Σ_Y which originates from the degree of freedom to choose the time evolution $(\mathcal{L}_{E_X}, \mathcal{L}_{E_Y})$ within the Pareto front of A_X and A_Y . As another constraint, Ref. [64] assumes the near-equilibrium condition and analytically derives the Nash equilibrium solution.

D. Examples

As an illustrative example, consider a graph $G(N, E)$ shown in Fig. 8(a). The time evolution is as follows: at time $t = 0$, the system is in state $(0, 0)$ with probability 1, and at time $t = \tau$, the system is in state $(2, 2)$ with probability 1. In this case, the path from node $(0, 0)$ to $(2, 2)$ that gives the value of the cost function $d_{E_X:E_Y}^s$ is unique for all s . Therefore, the Pareto front \mathcal{F}_A of partial activities is represented by

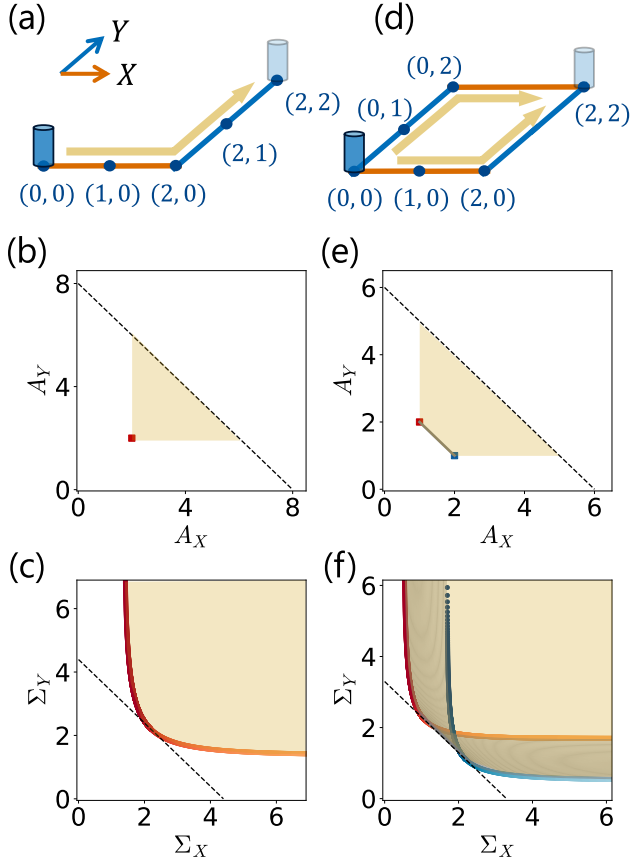


FIG. 8. Illustrative examples of the tradeoff relations between thermodynamic costs in finite-time processes. Consider the time evolution where probability 1 is transported from node $(0, 0)$ to $(2, 2)$. (a) and (d) illustrate the differences in the graph $G(N, E)$ where the dynamics takes place. (a) For any s , there is only one path that gives the value of the cost function $d_{E_X:E_Y}^s$. (d) There are two paths, and the path that gives the value of the cost function $d_{E_X:E_Y}^s$ varies depending on the value of s . (b) and (e) represent the Pareto front \mathcal{F}_A of partial activities for the time evolution on graphs (a) and (d), respectively. The black dotted line indicates the upper bound A_{XY} imposed on the activity when determining the partial EPs. (b) \mathcal{F}_A consists of a single red square. The parameter values are $\mathcal{W}_E = 4$, $\mathcal{W}_{E_X/E} = 2$, and $\mathcal{W}_{E_Y/E} = 2$. (e) \mathcal{F}_A is composed of a line segment. The parameter values are $\mathcal{W}_E = 3$, $\mathcal{W}_{E_X/E} = 1$, and $\mathcal{W}_{E_Y/E} = 1$. (c) and (f) illustrate the Pareto front \mathcal{F}_Σ of partial EPs for the time evolution on graphs (a) and (d), respectively. The black dotted line indicates the minimum value of the total EP. (c) The Pareto front \mathcal{F}_Σ is represented by a red curve, which is tangent to the black dotted line at one point. Here, $A_{XY} = 8$. (f) The Pareto front \mathcal{F}_Σ consists of parts of the red and blue curves and an edge with a slope of -1 , overlapping with the black dotted line. Here, $A_{XY} = 6$.

a single point, as shown in Fig. 8(b).

When \mathcal{F}_A has this form, setting $\mathcal{L}_{E_X} = \mathcal{W}_{E_X/E}$ and $\mathcal{L}_{E_Y} = \mathcal{W}_{E_Y/E}$ in Eq. (28) and then varying the thermodynamic forces provides the Pareto front \mathcal{F}_Σ of partial EPs (see Fig. 8(c)). The black dotted line represents the minimum value of the total EP, and the Pareto front \mathcal{F}_Σ is tangent to this

dotted line at a single point. From the shape of \mathcal{F}_Σ , it can be said that there exists a tradeoff relation between Σ_X and Σ_Y in the nonlinear regime. However, the cost of reducing the dissipation in one subsystem is not linear; the other subsystem must bear much more dissipation. This case will also be addressed in Sec. V.

Next, consider a graph $G(N, E)$ as shown in Fig. 8(d). Similarly to the previous example, the time evolution is as follows: at time $t = 0$, the system is in state $(0, 0)$ with probability 1, and at time $t = \tau$, the system is in state $(2, 2)$ with probability 1. There are two paths from node $(0, 0)$ to $(2, 2)$ that do not pass through the same node. In this case, the Pareto front \mathcal{F}_A of partial activities is as shown in Fig. 8(e). For $0 \leq s < 1/2$, only the counterclockwise path is optimal (blue square). Conversely, for $1/2 < s \leq 1$, only the clockwise path is optimal (red square). When $s = 1/2$, both paths are optimal. Furthermore, even taking the convex combination of these different paths, the transport cost remains optimal (gray edge).

As stated in Sec. IV C, since \mathcal{F}_A has an edge with a slope of -1 , \mathcal{F}_Σ also has an edge with the same slope (see Fig. 8(f)). This represents the minimum EP of the total system. Again, there is a tradeoff relation where reducing Σ_X increases Σ_Y . However, unlike the case in Fig. 8(c), the optimality of the total EP is always maintained along the edge. Therefore, the cost of reducing the dissipation in one subsystem is linear, and the other subsystem can simply bear the equivalent amount of increased dissipation.

V. OPTIMAL INFORMATION PROCESSING

In this section, we apply the results obtained so far to a simple information processing setup. In bipartite systems, we define the information flow, which quantitatively describes the exchange of information and formulate Maxwell's demon. Specifically, we consider a minimal four-state model of Maxwell's demon that performs measurement and feedback. We optimize the thermodynamic costs required for each information processing task and discuss the tradeoff relations between them. We also implement a protocol to achieve optimal information processing using double quantum dots.

A. Review: Information Flow and Maxwell's Demon

In a bipartite system, we introduce the concept of information flow. The mutual information between subsystems X and Y at time t is defined as [79]

$$I_{XY} = I_{X_t Y_t} := \sum_{x,y} p_{X_t Y_t}(x, y) \ln \frac{p_{X_t Y_t}(x, y)}{p_{X_t}(x) p_{Y_t}(y)}. \quad (31)$$

In bipartite systems, the time variation of mutual information can be decomposed into contributions from X and Y [58],

$$d_t I_{XY} = \dot{I}_X + \dot{I}_Y, \quad (32)$$

$$\dot{I}_X = \sum_{x>x',y} J_{xx'}^y \ln \frac{p_{Y_t|X_t}(y|x)}{p_{Y_t|X_t}(y|x')}, \quad (33)$$

$$\dot{I}_Y = \sum_{y>y',x} J_{yy'}^x \ln \frac{p_{X_t|Y_t}(x|y)}{p_{X_t|Y_t}(x|y')}, \quad (34)$$

where $p_{Y_t|X_t}(y|x) := p_{X_t Y_t}(x, y)/p_{X_t}(x)$ and $p_{X_t|Y_t}(x|y) := p_{X_t Y_t}(x, y)/p_{Y_t}(y)$ are the conditional probability distributions. The information flow of X , i.e., \dot{I}_X , corresponds to the change in mutual information due to the time evolution of X : $\dot{I}_X = \lim_{dt \rightarrow 0} (I_{X_{t+dt} Y_t} - I_{X_t Y_t})/dt$. The time integral of \dot{I}_X is denoted as ΔI_X . If $\Delta I_X > 0$, X is acquiring information by measuring Y . Conversely, if $\Delta I_X < 0$, X is either receiving feedback based on information about X or simply losing information. The same applies to \dot{I}_Y .

We now formulate Maxwell's demon. Ignoring the correlation with the other subsystem and focusing only on one subsystem may lead to an apparent violation of the second law of thermodynamics, as illustrated by the Szilard engine [53]. Ignoring the correlation with Y , the apparent EP rate of X , $\dot{\Sigma}_X^{\text{ap}}$, is given by

$$\dot{\Sigma}_X^{\text{ap}} := \sum_{x>x',y} J_{xx'}^y \ln \frac{p_{X_t}(x')}{p_{X_t}(x)} + \sum_{x>x',y} J_{xx'}^y \ln \frac{R_{xx'}^y}{R_{x'x}^y}. \quad (35)$$

The first term represents the change in Shannon entropy of X , whereas the second term represents the energy dissipation to the heat bath due to the transition of X . The EP rate $\dot{\Sigma}_X$ defined in Eq. (4) considers the correlation with Y , and its relation to the information flow is expressed as

$$\dot{\Sigma}_X = \dot{\Sigma}_X^{\text{ap}} - \dot{I}_X. \quad (36)$$

Therefore, if $\dot{I}_X < 0$, it is possible for $\dot{\Sigma}_X^{\text{ap}}$ to become negative, exhibiting Maxwell's demon. By taking into account the ignored correlation, i.e., the change in mutual information $-\dot{I}_X$, the second law is restored [54, 55, 80].

B. Optimal Measurement and Optimal Feedback

We consider a simple model of Maxwell's demon [81, 82], which consists of four states as shown in Fig. 9(a). In the corresponding graph $G(N, E)$, X and Y each take on states 0 or 1, and only transitions where either X or Y change are allowed. Also, the upper bound of the total activity is imposed. Since information processing is realized through transitions, this also limits the number of times information processing can occur.

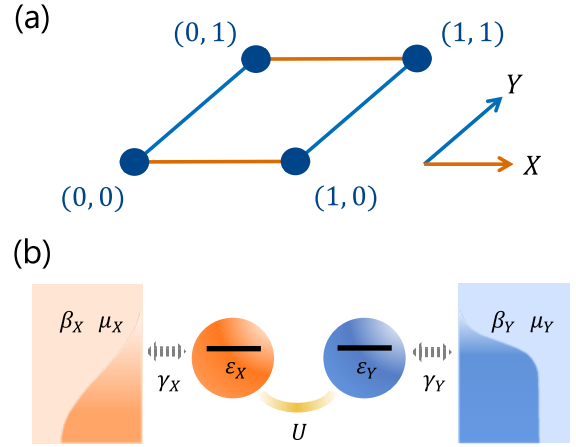


FIG. 9. (a) A four-state model. The states of the total system are specified by the states $x = 0, 1$ of subsystem X and $y = 0, 1$ of subsystem Y . There are no transitions where the states of X and Y change simultaneously, ensuring bipartiteness. (b) A schematic diagram of a double quantum dot that can be described by the model (a). Each dot X and Y is in contact with a thermal bath, with electrons entering and exiting a single energy level. In dot X (Y), the level being empty is represented by $x = 0$ ($y = 0$), and being occupied by an electron is represented by $x = 1$ ($y = 1$). The two dots are connected by capacitance, which creates interactions that enable feedback or measurement of the other dot.

To consider a process involving measurement and feedback, let the initial distribution be $p_{XY}^i = [1/2, 0, 1/2, 0]$ and the final distribution be $p_{XY}^f = [1/2, 1/2, 0, 0]$. Here, the probabilities of the states $r = (0, 0), (0, 1), (1, 0), (1, 1)$ are described in this order. In the initial distributions, the mutual information between X and Y is zero. During the time evolution from the initial distribution to the final distribution, the mutual information may increase depending on the intermediate states. This increase can be interpreted as a measurement taking place. Since the mutual information of the final distribution is again zero, the mutual information generated by the measurement is consumed through feedback (or loss of information). Using the method described in Sec. IV, the bound of the tradeoff relation between dissipation due to measurement and feedback can be determined.

The Pareto fronts of the partial activity and partial EP are shown in Fig. 10(a)(b). For any s , there are two paths from node $(1, 0)$ to $(0, 1)$ that give the value of the cost function d_{E_X, E_Y}^s , and the transport costs related to E_X and E_Y are the same for both paths. The shaded area in Fig. 10(a) represents the feasible region K_A for the partial activity, where the activity upper bound A_{XY} is satisfied. In the protocol giving the Pareto front \mathcal{F}_Σ (the red line in Fig. 10(b)) for partial EP, the partial activity takes the value on the red line in Fig. 10(a).

Since the geodesic of the Wasserstein distance is not necessarily unique, there exist processes with various changes in the mutual information. However, as long as the same ther-

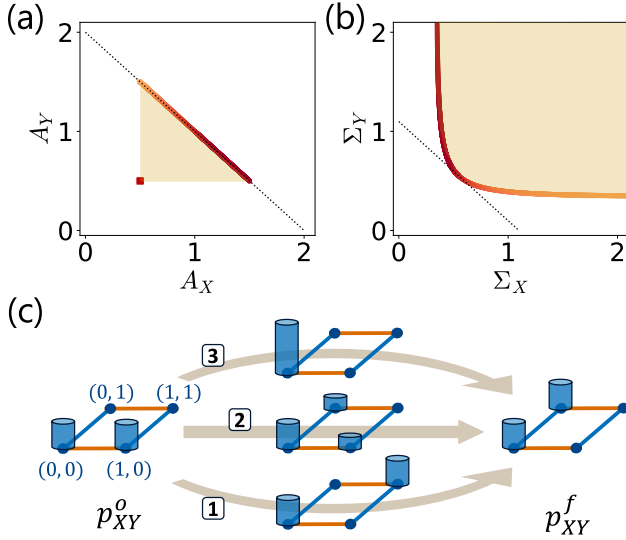


FIG. 10. Pareto front of the partial activity (a) and Pareto front of the partial EP (b) for the finite-time evolution $p_{XY}^o = [1/2, 0, 1/2, 0] \rightarrow p_{XY}^f = [1/2, 1/2, 0, 0]$. The parameter values are $\mathcal{W}_E = 1$, $\mathcal{W}_{E_X/E} = \mathcal{W}_{E_Y/E} = 1/2$, and $A_{XY} = 1.4$. (c) Differences in time evolution from the initial distribution p_{XY}^o to the final distribution p_{XY}^f . In method 1, the probability at node (1, 0) is first transported to node (1, 1) and then to node (0, 1). Conversely, in method 3, the probability at node (1, 0) is first transported to node (0, 0) and then to node (0, 1). In method 2, a small probability is transported from node (1, 0) to node (1, 1) while simultaneously transporting it to node (0, 1). The distributions on the arrows illustrate the probability distributions at $t = \tau/2$. In all cases, the transport cost remains the same. Thus, \mathcal{F}_A and \mathcal{F}_Σ are represented by (a) and (b), respectively. However, there are differences in how the mutual information changes.

mododynamic force is applied, the partial activity and partial EP remain unchanged. In other words, the Pareto fronts are identical in those processes. In the present model, we illustrate changes in the mutual information due to variations in the geodesic. To do this, we focus on the two paths that give the optimal transport cost (see Fig. 10(c)). Either path, or any combination of them, is optimal. There are numerous geodesics along these paths, among which we explain the three shown in Fig. 10(c).

1. Measurement-feedback separation

As a geodesic using only the path via node (1, 1), consider the following time evolution:

$$p_{X_t Y_t} = \begin{cases} \frac{1}{2}[1, 0, 1 - \frac{2t}{\tau}, \frac{2t}{\tau}] & (0 \leq t \leq \frac{\tau}{2}) \\ \frac{1}{2}[1, \frac{2t-\tau}{\tau}, 0, 1 - \frac{2t-\tau}{\tau}] & (\frac{\tau}{2} < t \leq \tau) \end{cases}. \quad (37)$$

This describes a situation where Y is measured for $0 \leq t \leq \tau/2$, and X is fed back for $\tau/2 < t \leq \tau$. In this case,

$\Delta I_X = -\ln 2$ and $\Delta I_Y = \ln 2$. Since measurement and feedback are temporally separated, we refer to this time evolution as measurement-feedback separation. The Pareto fronts of the partial activity and partial EP are represented as in Fig. 10(a)(b). Therefore, there is a tradeoff relation between the dissipation required for measurement and the dissipation required for feedback.

By increasing A_{XY} , which corresponds to the number of information processing steps, we observe changes in the feasibility and optimality of Maxwell's demon (see Fig. 11). First, to enable the finite-time evolution $p_{XY}^o \rightarrow p_{XY}^f$, it is necessary that $A_{XY} \geq \mathcal{W}_E$. Also, since $\Delta I_X = -\ln 2$, Maxwell's demon ($\Sigma_X^{\text{ap}} < 0$) can be realized if $\Sigma_X < \ln 2$. Now, considering the optimal protocol, we focus on the Pareto front \mathcal{F}_Σ of partial EPs (see Fig. 11(b)(d)(f)). When \mathcal{F}_Σ is realized, the partial activity takes values on the red or gray line segments (see Fig. 11(a)(c)(e)). On \mathcal{F}_Σ , Σ_X can be expressed using A_X as $2\mathcal{W}_{E_X/E} \tanh^{-1}(\mathcal{W}_{E_X/E}/A_X)$. Therefore, combined with $\mathcal{W}_{E_X/E} = 1/2$, $\Sigma_X < -\Delta I_X$ on \mathcal{F}_Σ if $A_X > 5/6$. When Σ_X is minimized, the partial activity of Y is $\mathcal{W}_{E_Y/E} = 1/2$. Thus, considering the partial activity of Y as well, the upper bound of the total activity required to realize Maxwell's demon is $A_{XY} > 5/6 + 1/2 = 4/3$. In the feasible region of the partial activity, Maxwell's demon can be realized in the red-shaded areas of Fig. 11(c)(e). When $1 \leq A_{XY} \leq 4/3$ as in Fig. 11(a)(b), Maxwell's demon cannot be realized at any thermodynamic costs.

Next, we consider the optimality of the total EP when realizing Maxwell's demon. As stated in Sec. IVC 1, when the total EP is minimized, the partial activity satisfies the relation $A_X/\mathcal{W}_{E_X/E} = A_Y/\mathcal{W}_{E_Y/E}$. The orange dashed lines in Fig. 11(a)(c)(e) represent this relation, and the orange dots correspond to the partial activity when the total EP is minimized. Therefore, to minimize the total EP while realizing Maxwell's demon, it is necessary that $A_Y > (\mathcal{W}_{E_Y/E}/\mathcal{W}_{E_X/E}) \cdot 5/6 = 5/6$. Thus, the upper bound of the total activity must be $A_{XY} > 5/6 + 5/6 = 5/3$. When $4/3 < A_{XY} \leq 5/3$ as in Fig. 11(c)(d), a protocol that minimizes the total EP cannot realize Maxwell's demon. Nevertheless, Maxwell's demon can be realized by increasing the dissipation Σ_Y in measurement and decreasing the dissipation Σ_X in feedback. When $A_{XY} > 5/3$ as in Fig. 11(e)(f), it is possible to realize Maxwell's demon while optimizing the total EP simultaneously.

In summary, to enable time evolution, it is necessary to have $A_{XY} \geq 1$, and to realize Maxwell's demon, $A_{XY} > 4/3$ is required. Furthermore, to minimize the total EP while realizing Maxwell's demon, $A_{XY} > 5/3$ is needed. By increasing A_{XY} , more diverse information processing becomes possible. This is because the total dissipation decreases, and according to the tradeoff relation, the dissipation in the subsystems can be further reduced. This is considered as a general property independent of the initial and final distributions or the graph.

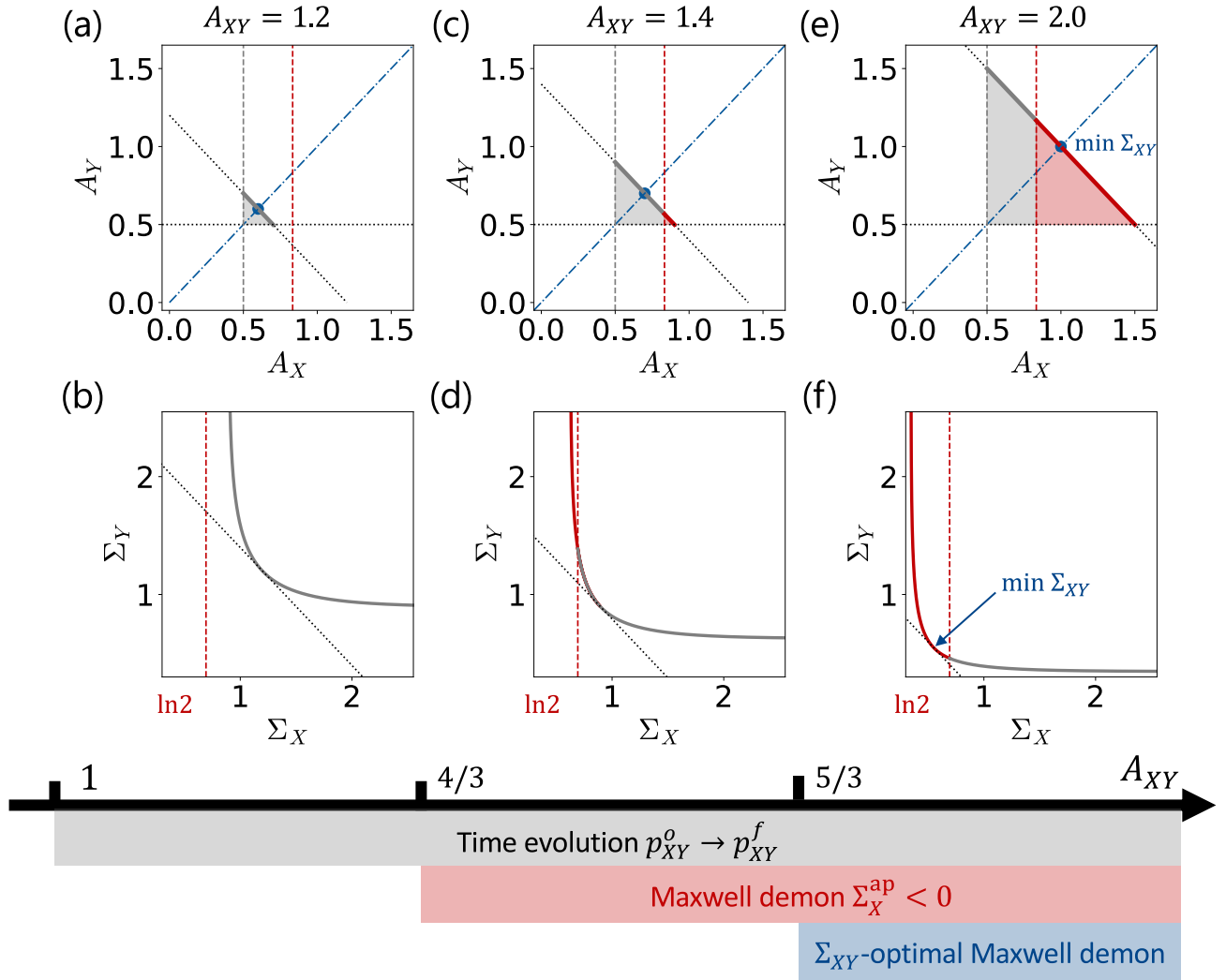


FIG. 11. Changes in the Pareto fronts \mathcal{F}_A and \mathcal{F}_Σ when increasing the upper bound of activity A_{XY} during the measurement-feedback separation (see Eq. (37)). In (a)(b), A_{XY} is set to 1.2, in (c)(d) to 1.4, and in (e)(f) to 2.0. In the $A_X - A_Y$ plane, the black diagonal dashed line represents the upper bound A_{XY} , the black horizontal dashed line represents \mathcal{W}_{E_Y} , and the gray vertical dashed line represents \mathcal{W}_{E_X} . The red vertical dashed line represents $A_X = \mathcal{W}_{E_X/E} \coth(-\Delta I_X/2\mathcal{W}_{E_X/E}) = 5/6$, indicating that Maxwell's demon for X is possible on the right side of this line. The orange dashed line represents $A_Y = (\mathcal{W}_{E_Y/E}/\mathcal{W}_{E_X/E})A_X$, and the point where this orange line intersects the A_{XY} dashed line is where the total EP is minimized (see also Fig. 7). In the $\Sigma_X - \Sigma_Y$ plane, the black diagonal dashed line represents the minimum EP of the total system. The Pareto front \mathcal{F}_Σ is tangent to this line at one point. In addition, the red vertical dashed line represents $-\Delta I_X = \ln 2$, indicating that Maxwell's demon for X is possible on the left side of this line.

2. Continuous measurement-feedback

Consider a different geodesic using the same path as in the Sec. VB 1:

$$\begin{aligned} p_{X_t Y_t} &= \left(1 - \frac{t}{\tau}\right) p_{XY}^o + \frac{t}{\tau} p_{XY}^f \\ &= \frac{1}{2} [1 - \epsilon, t/\tau, 1 - t/\tau, \epsilon], \end{aligned} \quad (38)$$

$$p_{X_{t+dt} Y_t} = p_{X_t Y_t} + \frac{dt}{2\tau} [0, 1, 0, -1], \quad (39)$$

$$p_{X_t Y_{t+dt}} = p_{X_t Y_t} + \frac{dt}{2\tau} [0, 0, -1, 1]. \quad (40)$$

Here, the time evolutions of X and Y in the Sec. VB 1 are performed simultaneously. However, to prevent the elements of $p_{X_{t+dt} Y_t}$ from becoming negative, we modify the initial distribution to $p_{XY}^o = [(1 - \epsilon)/2, 0, 1/2, \epsilon/2]$ ($\epsilon \ll 1$), ensuring $\epsilon > dt/\tau$ and keeping both values small. This correction does not change $\mathcal{W}_E, \mathcal{T}, \mathcal{W}_{E_X/E}$, or $\mathcal{W}_{E_Y/E}$. Therefore, the Pareto fronts of the partial activity and partial EP are still represented by Fig. 10(a)(b).

From the partial time evolution (Eqs. (39)(40)), the infor-

mation flow can be calculated, yielding

$$\dot{I}_X(t) = \frac{1}{2\tau} \ln \frac{\frac{t}{\tau}(1 - \frac{t}{\tau} + \epsilon)}{\epsilon(1 + \frac{t}{\tau} - \epsilon)}, \quad (41)$$

$$\dot{I}_Y(t) = \frac{1}{2\tau} \ln \frac{\epsilon(2 - \frac{t}{\tau} - \epsilon)}{(1 - \frac{t}{\tau})(\frac{t}{\tau} + \epsilon)} = -\dot{I}_X(\tau - t). \quad (42)$$

For $t/\tau < \epsilon$ and $t/\tau > 1 - \epsilon$, we have $\dot{I}_X < 0$, whereas for $\epsilon < t/\tau < 1 - \epsilon$, we have $\dot{I}_X > 0$. Unlike the measurement-feedback separation case discussed before, measurement and feedback are not temporally separated. Since measurement and feedback are continuously repeated, we refer to this time evolution as continuous measurement-feedback.

The change in the mutual information due to X and Y is entirely different from that in the measurement-feedback separation case:

$$\begin{aligned} \Delta I_X &= -\Delta I_Y \\ &= \frac{1}{2} \left(-(2 - \epsilon) \ln(2 - \epsilon) - 1 - \ln \epsilon - \epsilon \ln \epsilon \right. \\ &\quad \left. + (1 + \epsilon) \ln(1 + \epsilon) + (1 - \epsilon) \ln(1 - \epsilon) \right). \end{aligned} \quad (43)$$

The first and final terms contribute in the same way as the measurement-feedback separation case, which can be seen from simple calculations. Surprisingly, by making ϵ smaller, a larger information flow can be achieved. However, since $\Delta I_X > 0$ and $\Delta I_Y < 0$, the roles are reversed, with X performing the measurement and Y receiving the feedback. Therefore, when ϵ is sufficiently small, Maxwell's demon concerning Y can be realized, except in the region where $A_Y \simeq \mathcal{W}_{E_Y/E}$.

Since both the initial and final distributions are uncorrelated, $\Delta I = \Delta I_X + \Delta I_Y = 0$. In the limit $\epsilon \rightarrow 0$, the first and second terms in Eq. (43) converge to finite values, and the fourth and subsequent terms converge to zero. However, the third term contains $\ln \epsilon$, which diverges logarithmically. Nevertheless, because the transition rates implementing the time evolution are proportional to ϵ^{-1} (see Eq. (48)), it is practically impossible to make the information flow infinitely large.

3. Reset and redistribute

Finally, as a geodesic using only the path via node $(0, 0)$, consider the following time evolution:

$$p_{X_t Y_t} = \begin{cases} \frac{1}{2} [1 + \frac{2t}{\tau}, 0, 1 - \frac{2t}{\tau}, 0] & (0 \leq t \leq \frac{\tau}{2}) \\ \frac{1}{2} [1 - \frac{2t}{\tau}, \frac{2t}{\tau}, 0, 0] & (\frac{\tau}{2} < t \leq \tau) \end{cases}. \quad (44)$$

This describes a situation where, for $0 \leq t \leq \tau/2$, the state of X is reset to 0, and for $\tau/2 < t \leq \tau$, the state of Y is redistributed between 0 and 1. In this case, the mutual information does not change at all during the process, with $\Delta I_X = \Delta I_Y = 0$. Therefore, this is a process without any information processing.

4. Several remarks

From the perspective of transport, in Sec. VB 1, the probability $1/2$ was first moved to node $(1, 1)$ and then to node $(0, 1)$ (see also Fig. 10(c)). On the other hand, as in Sec. VB 2, it is also possible to move the probability directly to node $(0, 1)$. That is, a small probability can be transported simultaneously from node $(1, 0)$ to node $(1, 1)$ and from node $(1, 1)$ to node $(0, 1)$. Whichever the optimal transport matrix elements are sequentially transported or simultaneously transported, the trajectory of the time evolution remains geodesic. The difference in these geodesics results in different changes in the mutual information, but this is not due to moving the final distribution as discussed in Ref. [65].

We note that in this example, the Wasserstein distance and the total variation distance \mathcal{T} may differ because the graph $G(N, E)$ is not fully connected. In fact, for this initial and final distributions, $\mathcal{W}_E = 1$ and $\mathcal{T} = 1/2$, meaning that the bound using \mathcal{T} as in Ref. [49, 83] cannot be achieved.

It should be noted that optimization can similarly be performed for general initial and final distributions. For example, if $p_{XY}^o = [1, 0, 0, 0]$ and $p_{XY}^f = [1/2, 0, 0, 1/2]$, there exists a process where $\Delta I_X > 0$ and $\Delta I_Y > 0$. In this case, X and Y mutually measure each other, enhancing their correlation through information processing. We note that if $p_{XY}^o = [1/2, 0, 0, 1/2]$ and $p_{XY}^f = [1/2, 0, 1/2, 0]$, this represents the optimal bit erasure of a memory Y that stores the information of system X , reproducing the results of Ref. [49].

C. Implementation with Double Quantum Dots

The optimal information processing described above can be implemented using double quantum dots [81, 82, 84]. Consider a system as depicted in Fig. 9(b). The quantum dots X and Y are each coupled to thermal baths with inverse temperatures β_X and β_Y , and chemical potentials μ_X and μ_Y , respectively. Electrons can enter and exit the quantum dots from these thermal baths. We consider the low-temperature and Coulomb blockade regime. Thus, each dot cannot be occupied by more than one electron, and the dynamics can be treated as a Markov jump process. Using the state where dot X is empty ($x = 0$) as the reference energy, let ε_X be the energy of the state where X is occupied ($x = 1$). The same applies to dot Y . To introduce interaction between X and Y , the quantum dots are connected via capacitance. As a result, when both X and Y are occupied ($x = y = 1$), the total system energy, including the interaction energy U , becomes $\varepsilon_X + \varepsilon_Y + U$.

To implement optimal information processing, the transition rates are controlled. According to Fermi's golden rule,

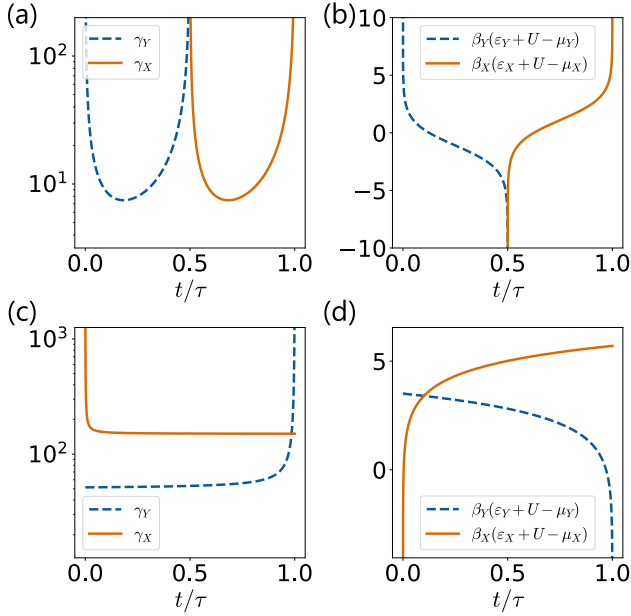


FIG. 12. Protocol for implementing optimal information processing with a double quantum dot. The upper bound of activity is set to $A_{XY} = 2.0$. The thermodynamic forces are chosen as $F_X = F_Y = 2 \tanh^{-1}(\mathcal{W}_E/A_{XY})$ to minimize the EP of the total system. Using the optimal transition rates, each parameter of the two quantum dots is calculated according to Eq. (45). Other parts of \mathcal{F}_Σ can be determined similarly. (a)(b) Measurement-feedback separation (see Eqs. (46)(47)). (c)(d) Continuous measurement-feedback (see Eq. (48)). Here, $\tau = 1$ and $\epsilon = 10^{-2}$.

the transition rates are given by

$$\begin{cases} R_{xx'}^y = \gamma_X f_X((x - x')(\epsilon_X + yU)) \\ R_{xy'}^y = \gamma_Y f_Y((y - y')(\epsilon_Y + xU)) \end{cases}, \quad (45)$$

where γ_X and γ_Y represent the coupling strengths with the thermal baths, and $f_X(\epsilon) := 1/(1 + e^{\beta_X(\epsilon - \mu_X)})$ and $f_Y(\epsilon) := 1/(1 + e^{\beta_Y(\epsilon - \mu_Y)})$ are the Fermi distribution functions. To implement optimal transport, it is necessary to manipulate the symmetric and antisymmetric parts of the transition rates in a time-dependent manner [38, 85]. In our quantum dot setup, this corresponds to adjusting the energy levels, interaction energy, and coupling strengths.

Henceforth, we will consider the foregoing protocols of information processing (Sec. VB 1, VB 2) separately. However, in each case, the protocol realizes the same Pareto front \mathcal{F}_Σ of partial EPs (Fig. 10(a)(b)).

1. Measurement-feedback separation

In *measurement-feedback separation*, we implement the protocol that realizes \mathcal{F}_Σ shown in Fig. 10(b). The time evolution is given by Eq. (37). During $0 \leq t \leq \tau/2$, the measurement transports probability $1/2$ to node $(1, 1)$, and dur-

ing $\tau/2 < t \leq \tau$, the feedback transports probability $1/2$ to node $(0, 1)$. The optimal transition rates for the measurement ($0 \leq t \leq \tau/2$) are given by

$$R_1^{10} = \frac{1}{1 - e^{-F_Y}} \frac{1}{\tau} \frac{1}{\frac{1}{2}(1 - \frac{2t}{\tau})}, R_1^{01} = \frac{1}{e^{F_Y} - 1} \frac{1}{\tau} \frac{1}{\frac{1}{2}\frac{2t}{\tau}}. \quad (46)$$

The first factor adjusts the reversibility of transitions on E_Y . The second factor is the transport rate per unit time (equal to $\dot{\mathcal{L}}_{E_Y}$), and the third factor is the reciprocal of the probability of the node from which the transport originates. In the optimal protocol, other transition rates are set to zero. This can be achieved by setting $\gamma_X = 0$ and $\beta_Y(\epsilon_Y - \mu_Y) \gg 1$.

Similarly, the optimal transition rates for the feedback ($\tau/2 < t \leq \tau$) are given by

$$R_{01}^1 = \frac{1}{1 - e^{-F_X}} \frac{1}{\tau} \frac{1}{\frac{1}{2}(1 - \frac{2t - \tau}{\tau})}, R_{10}^1 = \frac{1}{e^{F_X} - 1} \frac{1}{\tau} \frac{1}{\frac{1}{2}\frac{2t - \tau}{\tau}}. \quad (47)$$

Here again, in the optimal protocol, other transition rates are set to zero. This can be achieved by setting $\gamma_Y = 0$ and $\beta_X(\epsilon_X - \mu_X) \gg 1$.

Based on Eq. (45), the parameters of the quantum dots that implement the optimal protocol are shown in Fig. 12(a)(b). The thermodynamic forces F_X and F_Y are chosen to minimize the total EP. It is necessary to significantly change the parameters according to the changes in the node probabilities. Specifically, near $t = 0, \tau/2$, and τ , where the node probabilities become zero, the coupling strengths can become extremely large. In practice, it is necessary to slightly modify the initial and final distributions to ensure that the node probabilities do not become zero.

2. Continuous measurement-feedback

Next, in *continuous measurement-feedback*, we implement the protocol that realizes the same \mathcal{F}_Σ as in Sec. VC 1. The time evolution is given by Eq. (38). The optimal transition rates are given by

$$\begin{cases} R_{01}^1 = \frac{1}{1 - e^{-F_X}} \frac{1}{2\tau} \frac{1}{\frac{1}{2}\epsilon}, R_{10}^1 = \frac{1}{e^{F_X} - 1} \frac{1}{2\tau} \frac{1}{\frac{1}{2}\frac{t}{\tau}} \\ R_1^{10} = \frac{1}{1 - e^{-F_Y}} \frac{1}{2\tau} \frac{1}{\frac{1}{2}(1 - \frac{t}{\tau})}, R_1^{01} = \frac{1}{e^{F_Y} - 1} \frac{1}{2\tau} \frac{1}{\frac{1}{2}\epsilon} \end{cases}. \quad (48)$$

In the optimal protocol, other transition rates are set to zero. This can be achieved by setting $\beta_X(\epsilon_X - \mu_X) \gg 1, \beta_Y(\epsilon_Y - \mu_Y) \gg 1$. ϵ_X and ϵ_Y are manipulated satisfying this constraint. The protocol that minimizes the total EP is shown in Fig. 12(c)(d). Since the probability of node $(1, 1)$ is small and does not change significantly, the divergence observed near $t = \tau/2$ in Fig. 12(a)(b) can be avoided.

As described above, the optimal information processing can be implemented using double quantum dots. In general, when

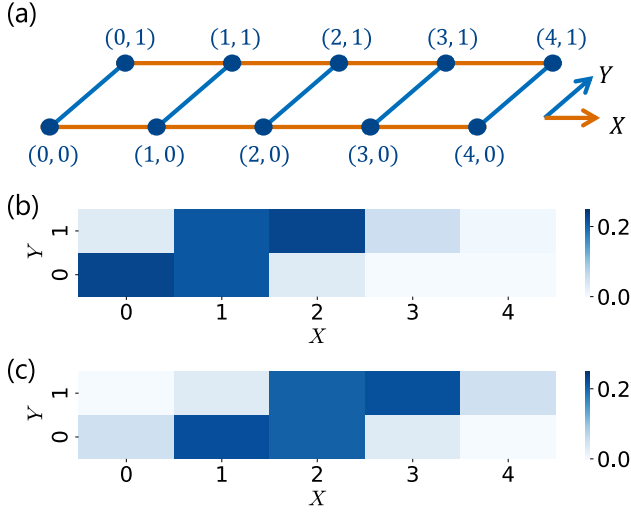


FIG. 13. (a) Model of *E. coli* chemotaxis. The autonomous transition rates are given as follows [86]. The methylation and demethylation rates are $R_{x+1,x}^0 = k_R$, $R_{x,x+1}^0 = \chi k_R$, $R_{x,x+1}^1 = k_B$, and $R_{x+1,x}^1 = \chi k_B$ for $x = 0, \dots, 3$. The activation and deactivation rates satisfy $R_x^{01} = R_x^{10} e^{2(1-x)+C}$ with $\min R_x^{01}, R_x^{10} = k_Y$ for $x = 0, \dots, 4$. The parameter χ adjusts the reverse reaction, and C describes the free energy's dependence on ligand concentration. We set $k_R = k_B = 1.0$, $k_Y = 0.010$, and $\chi = 0.10$. (b) Steady state for low ligand concentration ($C = 0$). This state is specified as the initial distribution, p_{XY}^o , with the value of $p_{XY}^o(x, y)$ shown by color in each cell. (c) State at time $t = \tau = 10$, where the initial distribution p_{XY}^o at $t = 0$ relaxes in response to a high ligand concentration signal ($C = 2.0$). This state is specified as the final distribution, p_{XY}^f , with $p_{XY}^f(x, y)$ values shown by color in each cell.

the probability on a node becomes small, such as near $t = 0$ and τ , large transition rates are required. This issue cannot be resolved by adjusting the thermodynamic forces. Moreover, it cannot be avoided by slowing down the rate of time evolution $\dot{\mathcal{L}}_E$. This is a bottleneck for achieving precise transport in discrete systems.

VI. APPLICATION TO MULTI-STATE SYSTEMS

In Secs. IV, V, we examined prototypical few-state systems to illustrate our results. However, our framework is not restricted to such situation but also immediately applicable to larger scale systems. In this section, we demonstrate its application to a multi-state model of chemotaxis.

We consider a model of *E. coli* chemotaxis [86, 87] as shown in Fig. 13(a). The state of X represents the receptor's methylation level, while the state of Y represents the kinase activity, where $y = 0$ and $y = 1$ correspond to the inactive and active states, respectively. The average value of X varies according to the environmental ligand concentration. Specifically, X tends to take smaller (larger) values at lower (higher) ligand concentrations (see Fig. 13(b)(c)). The change in Y oc-

curs much faster than in X , and in the (nonequilibrium) steady states, Y takes $y = 0$ and $y = 1$ with nearly equal probabilities, regardless of ligand concentration.

Consider the following adaptation situation. The system initially relaxes to the less methylated steady state (Fig. 13(b)), after which the ligand concentration suddenly increases. The subsystem Y responds rapidly to this signal, while subsystem X gradually relaxes to the highly methylated steady state (Fig. 13(c)). Eventually, the average value of Y , denoted as \bar{Y} , returns to a level near its original value prior to the signal (see also the dotted line in Fig. 14(a)). This adaptation is governed by autonomous transition rates that depend on both the methylation level and the ligand concentration (see the caption of Fig. 13 for details). These rates violate the detailed balance condition to maintain $\bar{Y} \simeq 0.5$, and thereby, chemical energy is continuously supplied to the system [86]. In this process ($0 \leq t \leq \tau$), the partial activities and entropy productions (EPs) for the autonomous transition rates are computed as $A_X = 11$, $A_Y = 1.5 \times 10^3$, $\Sigma_X^{\text{auto}} = 30$, and $\Sigma_Y^{\text{auto}} = 0.33$.

We examine the minimal cost required for the time evolution from the less methylated state p_{XY}^o (Fig. 13(b)) to the highly methylated state p_{XY}^f (Fig. 13(c)). The optimal time evolution is obtained by applying Eq. (28). Using the Python Optimal Transport library [88], we compute the optimal transport matrix, as shown in Fig. 14(b), and the Wasserstein distances as $\mathcal{W}_E = 0.90$, $\mathcal{W}_{E_X/E} = 0.87$, and $\mathcal{W}_{E_Y/E} = 0.030$. The Pareto fronts exhibit forms similar to those in Fig. 8(b)(c). Here, we consider the speed difference in the dynamics of X and Y , setting the thermodynamic forces and activity bounds so that the partial activities match their autonomous values, $A_X = 11$ and $A_Y = 1.5 \times 10^3$. The optimal time evolution is achieved by linearly interpolating between p_{XY}^o and p_{XY}^f , and thus the average values of X and Y also interpolates between its initial and final values (see Fig. 14(a)). The optimal protocol is determined from the optimal transport matrix (see Fig. 14(b)(c)). The optimal partial entropy productions (EPs) are $\Sigma_X = 0.14$ and $\Sigma_Y = 1.2 \times 10^{-6}$. The EP for X is reduced by a factor of more than 200 compared to the autonomous case, Σ_X^{auto} . The minimal cost for the time evolution itself is given by Σ_X , while Σ_X^{auto} accounts for the cost of implementing this evolution autonomously between steady states. Notably, the optimal time evolution does not involve a tradeoff between EP and adaptation accuracy [86]. On the other hand, the EP for Y is nearly zero in the optimal protocol, indicating that Y changes so rapidly that it remains almost equilibrated throughout the optimal time evolution.

Before concluding this section, we remark on the applicability to larger systems. We remember that the Wasserstein distance can be computed exactly for the examples discussed in this paper. For distributions with $|N|$ states, the exact calculation requires $\tilde{\mathcal{O}}(|N|^3)$ time steps [89], which is practically computable up to $|N| \simeq 10^4$. In even larger systems, the

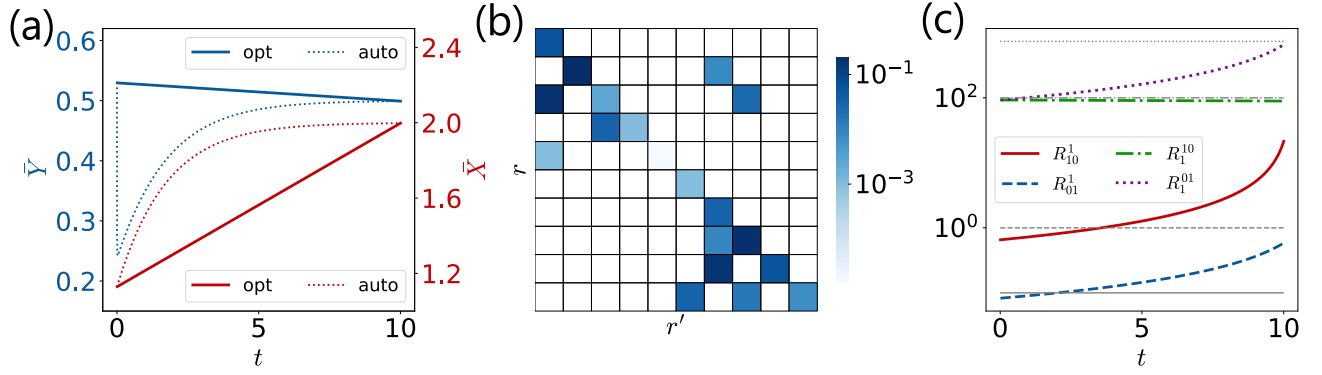


FIG. 14. (a) Time evolution of the average values of X and Y . The blue (red) solid line represents \bar{Y} (\bar{X}) in the optimal time evolution. The blue (red) dotted curve shows \bar{Y} (\bar{X}) in the time evolution driven by autonomous transition rates (see Fig. 13). In the autonomous process, \bar{Y} responds rapidly to the ligand signal and returns to approximately $\bar{Y} = 0.5$, indicating adaptation. (b) Optimal transport matrix Π^* within $\mathcal{U}(p_{XY}^f, p_{XY}^o)$ with respect to d_E . The values of $\Pi^*(r, r')$ are shown by color in each cell. Nodes $(0, 0), (0, 1), \dots, (1, 4)$ are labeled sequentially from top to bottom for r and from left to right for r' . (c) Protocol for implementing the optimal time evolution. Gray lines indicate the values of the autonomous transition rates. For ease of viewing, not all rates are shown.

Wasserstein distance can be approximated with $\tilde{\mathcal{O}}(|N|^2/\epsilon)$ time steps using the Sinkhorn algorithm [90, 91], where ϵ denotes the desired accuracy of the solution.

VII. CONCLUSION AND DISCUSSION

In this paper, we have introduced the concept of Pareto front for thermodynamic costs, revealing tradeoff relations between the costs associated with finite-time information processing (Eqs. (27)(28)). The primary focus of this paper is on discrete Markov jump processes, where we identified the optimal thermodynamic costs for each subsystem (Eqs. (19)(21)). To this end, we extended the Wasserstein distance to measure only the transport costs of subsystems such as the memory and the engine (Eq. (17)). We developed a general method for constructing the Pareto fronts for thermodynamic costs (Fig. 6, 7) and showed that the Pareto front of partial EPs is determined by the Pareto front of partial activities. We found that the non-uniqueness of the optimal transport matrix significantly affects the shapes of the Pareto fronts (Fig. 8). Our results imply that in the process of measurement and feedback, there is a tradeoff relation between the dissipation of measurement and that of feedback (Fig. 10). Increasing the activity enables more diverse information processing such as Maxwell's demon (Fig. 11). We also demonstrated that our results are applicable to the optimization of multi-state systems (Fig. 14). Below, we address some future perspectives.

Continuous systems.— In continuous systems such as Langevin systems, the activity is replaced by the diffusion constant, which typically cannot be controlled. Consequently, the tradeoff relation for thermodynamic costs in continuous systems fundamentally differs from those in discrete systems. For continuous systems, another recent paper [92] derived the

Pareto front of partial EPs using the L^2 Wasserstein distance and revealed the existence of the tradeoff relation between EPs. On the other hand, taking the continuous limit of Eq. (19) would yield an L^1 inequality, which cannot be achieved in general [38, 39].

More practical situations.— Optimizing the thermodynamic costs of information processing has various potential applications. For instance, current industrial computational devices exhibit thermal dissipation much larger than the fundamental bound. It is thus crucial to understand the extent to which computational costs can be fundamentally reduced in such devices [93, 94]. Applications to biological systems are also highly intriguing. In cells, various chemical reactions occur to maintain life, consuming free energy in the process. These reactions and processes are subject to thermodynamic constraints due to thermal fluctuations in the environment [95]. Additionally, biological constraints introduce various tradeoff relations between functionality and cost, such as in sensory adaptation [96, 97], kinetic proofreading [98, 99], and biochemical copying [100].

The minimal costs and tradeoff relations obtained through our method can be considered as an important step toward optimization and functional understanding in such systems. However, optimization using optimal transport theory assumes full control, requiring the ability to arbitrarily manipulate transition rates. In realistic systems, however, the time dependence of transition rates can only be partially controlled. Therefore, to establish more relevant bounds to those situations, it would be necessary to explore the optimization of thermodynamic costs under limited control [101, 102].

ACKNOWLEDGMENTS

We thank Sosuke Ito for the fruitful discussion. This work is supported by JST ERATO Grant No. JPMJER2302, Japan. T.K. is supported by World-leading Innovative Graduate Study Program for Materials Research, Informa-

tion, and Technology (MERIT-WINGS) of the University of Tokyo. T.K. is also supported by JSPS KAKENHI Grant No. JP24KJ0611. K.F. acknowledges support from JSPS KAKENHI (Grant Nos. JP23K13036 and JP24H00831). T.S. is supported by JSPS KAKENHI Grant No. JP19H05796 and JST CREST Grant No. JPMJCR20C1. T.S. is also supported by Institute of AI and Beyond of the University of Tokyo.

* kamijima@noneq.t.u-tokyo.ac.jp

- [1] K. Sekimoto, *Stochastic energetics*, Vol. 799 (Springer, 2010).
- [2] U. Seifert, Stochastic thermodynamics, fluctuation theorems and molecular machines, *Rep. Prog. Phys.* **75**, 126001 (2012).
- [3] L. Peliti and S. Pigolotti, *Stochastic thermodynamics: an introduction* (Princeton University Press, 2021).
- [4] S. Ciliberto, Experiments in stochastic thermodynamics: Short history and perspectives, *Phys. Rev. X* **7**, 021051 (2017).
- [5] F. L. Curzon and B. Ahlborn, Efficiency of a carnot engine at maximum power output, *Am. J. Phys.* **43**, 22 (1975).
- [6] C. van den Broeck, Thermodynamic efficiency at maximum power, *Phys. Rev. Lett.* **95**, 190602 (2005).
- [7] T. Schmiedl and U. Seifert, Optimal finite-time processes in stochastic thermodynamics, *Phys. Rev. Lett.* **98**, 108301 (2007).
- [8] G. E. Crooks, Measuring thermodynamic length, *Phys. Rev. Lett.* **99**, 100602 (2007).
- [9] M. Esposito, R. Kawai, K. Lindenberg, and C. Van den Broeck, Efficiency at maximum power of low-dissipation carnot engines, *Phys. Rev. Lett.* **105**, 150603 (2010).
- [10] D. A. Sivak and G. E. Crooks, Thermodynamic metrics and optimal paths, *Phys. Rev. Lett.* **108**, 190602 (2012).
- [11] S. Blaber and D. A. Sivak, Optimal control in stochastic thermodynamics, *Journal of Physics Communications* **7**, 033001 (2023).
- [12] Y.-H. Ma, R.-X. Zhai, J. Chen, C. P. Sun, and H. Dong, Experimental test of the $1/\tau$ -scaling entropy generation in finite-time thermodynamics, *Phys. Rev. Lett.* **125**, 210601 (2020).
- [13] N. Shiraishi, K. Funo, and K. Saito, Speed limit for classical stochastic processes, *Phys. Rev. Lett.* **121**, 070601 (2018).
- [14] S. Ito, Stochastic thermodynamic interpretation of information geometry, *Phys. Rev. Lett.* **121**, 030605 (2018).
- [15] S. Ito and A. Dechant, Stochastic time evolution, information geometry, and the cramér-rao bound, *Phys. Rev. X* **10**, 021056 (2020).
- [16] G. Falasco and M. Esposito, Dissipation-time uncertainty relation, *Phys. Rev. Lett.* **125**, 120604 (2020).
- [17] R. Hamazaki, Speed limits for macroscopic transitions, *PRX Quantum* **3**, 020319 (2022).
- [18] A. C. Barato and U. Seifert, Thermodynamic uncertainty relation for biomolecular processes, *Phys. Rev. Lett.* **114**, 158101 (2015).
- [19] T. R. Gingrich, J. M. Horowitz, N. Perunov, and J. L. England, Dissipation bounds all steady-state current fluctuations, *Phys. Rev. Lett.* **116**, 120601 (2016).
- [20] P. Pietzonka, A. C. Barato, and U. Seifert, Universal bound on the efficiency of molecular motors, *J. Stat. Mech.* (2016) 124004.
- [21] N. Shiraishi, K. Saito, and H. Tasaki, Universal trade-off relation between power and efficiency for heat engines, *Phys. Rev. Lett.* **117**, 190601 (2016).
- [22] K. Proesmans and C. Van den Broeck, Discrete-time thermodynamic uncertainty relation, *EPL* **119**, 20001 (2017).
- [23] C. Maes, Frenetic bounds on the entropy production, *Phys. Rev. Lett.* **119**, 160601 (2017).
- [24] A. Dechant, Multidimensional thermodynamic uncertainty relations, *J. Phys. A Math. Theor.* **52**, 035001 (2018).
- [25] K. Brandner, T. Hanazato, and K. Saito, Thermodynamic bounds on precision in ballistic multiterminal transport, *Phys. Rev. Lett.* **120**, 090601 (2018).
- [26] P. Pietzonka and U. Seifert, Universal trade-off between power, efficiency, and constancy in steady-state heat engines, *Phys. Rev. Lett.* **120**, 190602 (2018).
- [27] Y. Hasegawa and T. Van Vu, Uncertainty relations in stochastic processes: An information inequality approach, *Phys. Rev. E* **99**, 062126 (2019).
- [28] T. Koyuk and U. Seifert, Thermodynamic uncertainty relation for time-dependent driving, *Phys. Rev. Lett.* **125**, 260604 (2020).
- [29] K. Liu, Z. Gong, and M. Ueda, Thermodynamic uncertainty relation for arbitrary initial states, *Phys. Rev. Lett.* **125**, 140602 (2020).
- [30] S. Otsubo, S. Ito, A. Dechant, and T. Sagawa, Estimating entropy production by machine learning of short-time fluctuating currents, *Phys. Rev. E* **101**, 062106 (2020).
- [31] C. Villani, *Optimal transport: old and new*, Vol. 338 (Springer, 2009).
- [32] G. Peyré and M. Cuturi, Computational optimal transport: With applications to data science, *Foundations and Trends® in Machine Learning* **11**, 355 (2019).
- [33] E. Aurell, C. Mejía-Monasterio, and P. Muratore-Ginanneschi, Optimal protocols and optimal transport in stochastic thermodynamics, *Phys. Rev. Lett.* **106**, 250601 (2011).
- [34] E. Aurell, K. Gawędzki, C. Mejía-Monasterio, R. Mohayadee, and P. Muratore-Ginanneschi, Refined second law of thermodynamics for fast random processes, *Journal of statistical physics* **147**, 487 (2012).
- [35] A. Dechant and Y. Sakurai, Thermodynamic interpretation of wasserstein distance, *arXiv preprint arXiv:1912.08405* (2019).
- [36] M. Nakazato and S. Ito, Geometrical aspects of entropy production in stochastic thermodynamics based on wasserstein distance, *Phys. Rev. Res.* **3**, 043093 (2021).
- [37] P. Muratore-Ginanneschi, C. Mejía-Monasterio, and L. Peliti,

- Heat release by controlled continuous-time markov jump processes, *Journal of Statistical Physics* **150**, 181 (2013).
- [38] A. Dechant, Minimum entropy production, detailed balance and wasserstein distance for continuous-time markov processes, *J. Phys. A* **55**, 094001 (2022).
- [39] T. Van Vu and K. Saito, Thermodynamic unification of optimal transport: Thermodynamic uncertainty relation, minimum dissipation, and thermodynamic speed limits, *Phys. Rev. X* **13**, 011013 (2023).
- [40] T. Van Vu and K. Saito, Topological speed limit, *Phys. Rev. Lett.* **130**, 010402 (2023).
- [41] R. Landauer, Information is physical, *Physics Today* **44**, 23 (1991).
- [42] M. Esposito and C. Van den Broeck, Second law and landauer principle far from equilibrium, *Europhysics Letters* **95**, 40004 (2011).
- [43] A. Bérut, A. Arakelyan, A. Petrosyan, S. Ciliberto, R. Dillenschneider, and E. Lutz, Experimental verification of landauer's principle linking information and thermodynamics, *Nature* **483**, 187 (2012).
- [44] Y. Jun, M. c. v. Gavrilo, and J. Bechhoefer, High-precision test of landauer's principle in a feedback trap, *Phys. Rev. Lett.* **113**, 190601 (2014).
- [45] J. Hong, B. Lambson, S. Dhuey, and J. Bokor, Experimental test of landauer's principle in single-bit operations on nanomagnetic memory bits, *Science Advances* **2**, e1501492 (2016).
- [46] S. Dago, J. Pereda, N. Barros, S. Ciliberto, and L. Bellon, Information and thermodynamics: Fast and precise approach to landauer's bound in an underdamped micromechanical oscillator, *Phys. Rev. Lett.* **126**, 170601 (2021).
- [47] K. Proesmans, J. Ehrich, and J. Bechhoefer, Finite-time landauer principle, *Phys. Rev. Lett.* **125**, 100602 (2020).
- [48] Y.-Z. Zhen, D. Egloff, K. Modi, and O. Dahlsten, Universal bound on energy cost of bit reset in finite time, *Phys. Rev. Lett.* **127**, 190602 (2021).
- [49] J. S. Lee, S. Lee, H. Kwon, and H. Park, Speed limit for a highly irreversible process and tight finite-time landauer's bound, *Phys. Rev. Lett.* **129**, 120603 (2022).
- [50] T. Van Vu and K. Saito, Finite-time quantum landauer principle and quantum coherence, *Phys. Rev. Lett.* **128**, 010602 (2022).
- [51] M. Scandi, D. Barker, S. Lehmann, K. A. Dick, V. F. Maisi, and M. Perarnau-Llobet, Minimally dissipative information erasure in a quantum dot via thermodynamic length, *Phys. Rev. Lett.* **129**, 270601 (2022).
- [52] J. M. Parrondo, J. M. Horowitz, and T. Sagawa, Thermodynamics of information, *Nature physics* **11**, 131 (2015).
- [53] H. Leff and A. F. Rex, *Maxwell's Demon 2 Entropy, Classical and Quantum Information, Computing* (CRC Press, 2002).
- [54] T. Sagawa and M. Ueda, Second law of thermodynamics with discrete quantum feedback control, *Phys. Rev. Lett.* **100**, 080403 (2008).
- [55] T. Sagawa and M. Ueda, Minimal energy cost for thermodynamic information processing: Measurement and information erasure, *Phys. Rev. Lett.* **102**, 250602 (2009).
- [56] T. Sagawa and M. Ueda, Generalized jarzynski equality under nonequilibrium feedback control, *Phys. Rev. Lett.* **104**, 090602 (2010).
- [57] S. Ito and T. Sagawa, Information thermodynamics on causal networks, *Phys. Rev. Lett.* **111**, 180603 (2013).
- [58] J. M. Horowitz and M. Esposito, Thermodynamics with continuous information flow, *Phys. Rev. X* **4**, 031015 (2014).
- [59] S. Toyabe, T. Sagawa, M. Ueda, E. Muneyuki, and M. Sano, Experimental demonstration of information-to-energy conversion and validation of the generalized jarzynski equality, *Nature physics* **6**, 988 (2010).
- [60] J. V. Koski, V. F. Maisi, T. Sagawa, and J. P. Pekola, Experimental observation of the role of mutual information in the nonequilibrium dynamics of a maxwell demon, *Phys. Rev. Lett.* **113**, 030601 (2014).
- [61] M. Ribezzi-Crivellari and F. Ritort, Large work extraction and the landauer limit in a continuous maxwell demon, *Nature Physics* **15**, 660 (2019).
- [62] D. Abreu and U. Seifert, Extracting work from a single heat bath through feedback, *Europhysics Letters* **94**, 10001 (2011).
- [63] A. Taghvaei, O. M. Miangolarra, R. Fu, Y. Chen, and T. T. Georgiou, On the relation between information and power in stochastic thermodynamic engines, *IEEE Control Systems Letters* **6**, 434 (2022).
- [64] Y. Fujimoto and S. Ito, Game-theoretical approach to minimum entropy productions in information thermodynamics, *Phys. Rev. Res.* **6**, 013023 (2024).
- [65] R. Nagase and T. Sagawa, Thermodynamically optimal information gain in finite-time measurement, *Phys. Rev. Res.* **6**, 033239 (2024).
- [66] N. G. Van Kampen, *Stochastic processes in physics and chemistry*, Vol. 1 (Elsevier, 1992).
- [67] C. Gardiner, *Stochastic methods*, Vol. 4 (Springer Berlin, 2009).
- [68] D. Hartich, A. C. Barato, and U. Seifert, Stochastic thermodynamics of bipartite systems: transfer entropy inequalities and a maxwell's demon interpretation, *Journal of Statistical Mechanics: Theory and Experiment* **2014**, P02016 (2014).
- [69] C. Maes, Frenesy: Time-symmetric dynamical activity in nonequilibria, *Physics Reports* **850**, 1 (2020).
- [70] N. Shiraishi and T. Sagawa, Fluctuation theorem for partially masked nonequilibrium dynamics, *Phys. Rev. E* **91**, 012130 (2015).
- [71] T. Van Vu and Y. Hasegawa, Unified thermodynamic-kinetic uncertainty relation, *Journal of Physics A: Mathematical and Theoretical* **55**, 405004 (2022).
- [72] V. N. Sudakov, *Geometric problems in the theory of infinite-dimensional probability distributions*, 141 (American Mathematical Soc., 1979).
- [73] P. Ngatchou, A. Zarei, and A. El-Sharkawi, Pareto multi objective optimization, in *Proceedings of the 13th International Conference on, Intelligent Systems Application to Power Systems* (IEEE, 2005) pp. 84–91.
- [74] C. Coello, *Evolutionary Algorithms for solving Multi-Objective Problems* (Springer, 2007).
- [75] G. Benenti, G. Casati, K. Saito, and R. Whitney, Fundamental aspects of steady-state conversion of heat to work at the nanoscale, *Phys. Rep.* **694**, 1 (2017).
- [76] A. P. Solon and J. M. Horowitz, Phase transition in protocols minimizing work fluctuations, *Phys. Rev. Lett.* **120**, 180605 (2018).

- [77] Y. Ashida and T. Sagawa, Learning the best nanoscale heat engines through evolving network topology, *Commun. Phys.* **4**, 45 (2021).
- [78] R. T. Marler and J. S. Arora, The weighted sum method for multi-objective optimization: new insights, *Structural and multidisciplinary optimization* **41**, 853 (2010).
- [79] T. M. Cover, *Elements of information theory* (John Wiley & Sons, 1999).
- [80] T. Sagawa and M. Ueda, Role of mutual information in entropy production under information exchanges, *New Journal of Physics* **15**, 125012 (2013).
- [81] P. Strasberg, G. Schaller, T. Brandes, and M. Esposito, Thermodynamics of a physical model implementing a maxwell demon, *Phys. Rev. Lett.* **110**, 040601 (2013).
- [82] G. Diana and M. Esposito, Mutual entropy production in bipartite systems, *Journal of Statistical Mechanics: Theory and Experiment* **2014**, P04010 (2014).
- [83] D. S. P. Salazar, Lower bound for entropy production rate in stochastic systems far from equilibrium, *Phys. Rev. E* **106**, L032101 (2022).
- [84] A. Kutvonen, T. Sagawa, and T. Ala-Nissila, Thermodynamics of information exchange between two coupled quantum dots, *Phys. Rev. E* **93**, 032147 (2016).
- [85] B. Remlein and U. Seifert, Optimality of nonconservative driving for finite-time processes with discrete states, *Phys. Rev. E* **103**, L050105 (2021).
- [86] G. Lan, P. Sartori, S. Neumann, V. Sourjik, and Y. Tu, The energy–speed–accuracy trade-off in sensory adaptation, *Nature physics* **8**, 422 (2012).
- [87] P. Sartori, L. Granger, C. F. Lee, and J. M. Horowitz, Thermodynamic costs of information processing in sensory adaptation, *PLoS computational biology* **10**, e1003974 (2014).
- [88] R. Flamary, N. Courty, A. Gramfort, M. Z. Alaya, A. Boissunon, S. Chambon, L. Chapel, A. Corenflos, K. Fatras, N. Fournier, L. Gautheron, N. T. Gayraud, H. Janati, A. Rakotomamonjy, I. Redko, A. Rolet, A. Schutz, V. Seguy, D. J. Sutherland, R. Tavenard, A. Tong, and T. Vayer, Pot: Python optimal transport, *Journal of Machine Learning Research* **22**, 1 (2021).
- [89] O. Pele and M. Werman, Fast and robust earth mover’s distances, in *2009 IEEE 12th international conference on computer vision* (IEEE, 2009) pp. 460–467.
- [90] M. Cuturi, Sinkhorn distances: Lightspeed computation of optimal transport, *Advances in neural information processing systems* **26** (2013).
- [91] K. Pham, K. Le, N. Ho, T. Pham, and H. Bui, On unbalanced optimal transport: An analysis of Sinkhorn algorithm, in *International Conference on Machine Learning* (PMLR, 2020) pp. 7673–7682.
- [92] T. Kamijima, A. Takatsu, K. Funo, and T. Sagawa, Optimal finite-time maxwell’s demons in langevin systems, *arXiv preprint arXiv:2410.11603* (2024).
- [93] D. H. Wolpert, The stochastic thermodynamics of computation, *Journal of Physics A: Mathematical and Theoretical* **52**, 193001 (2019).
- [94] N. Freitas, J.-C. Delvenne, and M. Esposito, Stochastic thermodynamics of nonlinear electronic circuits: A realistic framework for computing around kt , *Phys. Rev. X* **11**, 031064 (2021).
- [95] R. Rao and M. Esposito, Nonequilibrium thermodynamics of chemical reaction networks: Wisdom from stochastic thermodynamics, *Phys. Rev. X* **6**, 041064 (2016).
- [96] G. Lan, P. Sartori, S. Neumann, V. Sourjik, and Y. Tu, The energy–speed–accuracy trade-off in sensory adaptation, *Nature physics* **8**, 422 (2012).
- [97] S. Ito and T. Sagawa, Maxwell’s demon in biochemical signal transduction with feedback loop, *Nature communications* **6**, 1 (2015).
- [98] A. Murugan, D. A. Huse, and S. Leibler, Speed, dissipation, and error in kinetic proofreading, *Proceedings of the National Academy of Sciences* **109**, 12034 (2012).
- [99] P. Sartori and S. Pigolotti, Thermodynamics of error correction, *Phys. Rev. X* **5**, 041039 (2015).
- [100] T. E. Ouldridge, C. C. Govern, and P. R. ten Wolde, Thermodynamics of computational copying in biochemical systems, *Phys. Rev. X* **7**, 021004 (2017).
- [101] A. Kolchinsky and D. H. Wolpert, Work, entropy production, and thermodynamics of information under protocol constraints, *Phys. Rev. X* **11**, 041024 (2021).
- [102] A. Zhong and M. R. DeWeese, Limited-control optimal protocols arbitrarily far from equilibrium, *Phys. Rev. E* **106**, 044135 (2022).

Supplemental Material for “Finite-time thermodynamic bounds and tradeoff relations for information processing”

S1. SUPPLEMENTAL TO SECTION III

Here, we supplement the proofs and discussions omitted in Sec. III.

A. Correspondence between Transition Rates and Transport Matrices

We consider an infinitesimal time evolution from $p_{X_t Y_t}$ to $p_{X_{t+dt} Y_{t+dt}}$, where $\mathcal{W}_E(p_{X_{t+dt} Y_{t+dt}}, p_{X_t Y_t}) = \mathcal{O}(dt)$ and terms of $\mathcal{O}(dt)$ are neglected. The transition rates $R : p_{X_t Y_t} \rightarrow p_{X_{t+dt} Y_{t+dt}}$ that realize this time evolution satisfy Eq. (2). These transition rates have nonzero values only on E . In this subsection, we explain the procedure for establishing a correspondence between the transport matrix within $\mathcal{U}(p_{X_{t+dt} Y_{t+dt}}, p_{X_t Y_t})$ and the transition rates that realize the time evolution $p_{X_t Y_t} \rightarrow p_{X_{t+dt} Y_{t+dt}}$ following Ref. [S1]. As will be shown later, this correspondence allows for the optimization of the transition rates to be equivalent to the optimization of the transport matrices when minimizing the partial activity rate. Here, we use the cost function d_E , but the same applies when using d_{E_X} , $d_{E_X/E}$, and $d_{E_X:E_Y}^s$.

First, we construct the transition rates from the transport matrix. We choose an arbitrary transport matrix $\hat{\Pi}$ that is an element of $\mathcal{U}(p_{X_{t+dt} Y_{t+dt}}, p_{X_t Y_t})$, where the off-diagonal elements are $\mathcal{O}(dt)$. Given that $\mathcal{W}_E(p_{X_{t+dt} Y_{t+dt}}, p_{X_t Y_t}) = \mathcal{O}(dt)$, such a transport matrix always exists. In general, $\hat{\Pi}$ has nonzero values for elements that are not on E , making it unsuitable for direct conversion to transition rates. Therefore, we transform the transport matrix so that it belongs to $\mathcal{U}(p_{X_{t+dt} Y_{t+dt}}, p_{X_t Y_t})$ and retains the transport cost concerning d_E , while only having nonzero values on E and the diagonal elements. To achieve this, we repeatedly apply the following procedures for all $\hat{\Pi}(r, r') > 0$ where $[r, r'] \notin E$ (i.e., $d_E(r, r') > 1$). 0. Select a path $r' = r_0 \rightarrow r_1 \rightarrow \dots \rightarrow r_m = r$ that connects node r' to r and gives the minimal $l_E = m$.

1. $\hat{\Pi}(r_{i+1}, r_i) \rightarrow \hat{\Pi}(r_{i+1}, r_i) + \hat{\Pi}(r, r') \ (i = 0, \dots, m-1)$.
2. $\hat{\Pi}(r_i, r_i) \rightarrow \hat{\Pi}(r_i, r_i) - \hat{\Pi}(r, r') \ (i = 1, \dots, m-1)$.
3. $\hat{\Pi}(r, r') \rightarrow 0$.

In procedure (1), the transport $\hat{\Pi}(r, r') > 0$ that cannot be performed on the edge is divided along the shortest path from node r' to r . Since d_E is linear, the transport cost does not change in this procedure. In procedure (2), at nodes along the shortest path, the probability of not transporting (diagonal elements) is reduced by the amount transported to the next node. The transport matrix transformed by such procedures is denoted as Π , which satisfies $\Pi \in \mathcal{U}(p_{X_{t+dt} Y_{t+dt}}, p_{X_t Y_t})$. Moreover, the transport cost also remains unchanged: $\sum_{r, r'} d_E(r, r') \hat{\Pi}(r, r') = \sum_{r, r'} d_E(r, r') \Pi(r, r')$.

In general, the shortest path between nodes is not unique, so Π generated from $\hat{\Pi}$ is also not necessarily unique. Moreover, in procedure (2), if the diagonal element of an intermediate node is originally zero, this may become negative after the transformation. In this case, a small amount ϵ is in advance allocated to the probability of the intermediate node. Since the off-diagonal elements are $\mathcal{O}(dt)$, the non-negativity of the transport matrix is preserved as $dt \rightarrow 0$. Simultaneously, by maintaining $\epsilon \gg dt$ while letting $\epsilon \rightarrow 0$, the Wasserstein distance remains unaffected. When transforming a general transport matrix, the transport amount $\hat{\Pi}(r, r')$ is not $\mathcal{O}(dt)$, so this method cannot be used, and the diagonal elements may become negative. Therefore, to avoid this problem in the case of finite-time evolution, the transformation should be applied to the transport matrix for the infinitesimal time evolution at each time step.

Given that Π has nonzero values only on the edges of E , we can construct the transition rates $R : p_{X_t Y_t} \rightarrow p_{X_{t+dt} Y_{t+dt}}$ based on this:

$$R(r, r') = \begin{cases} \frac{\Pi(r, r')}{p_{X_t Y_t}(r') dt} & ([r, r'] \in E) \\ 0 & ([r, r'] \notin E) \end{cases}. \quad (\text{S1})$$

By doing so, R realizes the time evolution from $p_{X_t Y_t}$ to $p_{X_{t+dt} Y_{t+dt}}$.

Conversely, we now construct the transport matrix from the transition rate. Choose arbitrary transition rates $R : p_{X_t Y_t} \rightarrow p_{X_{t+dt} Y_{t+dt}}$. Define the transport matrix Π as follows:

$$\Pi(r, r') = \begin{cases} R(r, r') p_{X_t Y_t}(r') dt & ([r, r'] \in E) \\ 0 & ([r, r'] \notin E) \\ (1 - \sum_{r'' (\neq r)} W(r'', r) dt) p_{X_t Y_t}(r) & (r = r') \end{cases} \quad (\text{S2})$$

As $dt \rightarrow 0$, the diagonal elements are guaranteed to be nonnegative, ensuring that $\Pi \in \mathcal{U}(p_{X_{t+dt} Y_{t+dt}}, p_{X_t Y_t})$. We note that the transport matrix Π constructed in this manner has nonzero values only on E and the diagonal elements.

B. Explicit Form of Optimal Protocols

Here, we explicitly provide the optimal protocols discussed in the main text. We only show the case of the total system (Sec. II C) for simplicity following Ref. [S1], but the protocols for subsystems (Sec. III, IV) can be constructed in a similar way.

The transition rates R that realize the minimum value in Eq. (7) can be expressed using the optimal transport matrix $\Pi^* \in \mathcal{U}(p_{X_{t+dt} Y_{t+dt}}, p_{X_t Y_t})$ with respect to d_E as $R(r, r') p_{X_t Y_t}(r') dt = \Pi^*(r, r')$ for $[r, r'] \in E$. However, in general, Π^* obtained by solving the optimal transport problem may have nonzero values on edges not included in E . Therefore, it is necessary to transform Π^* so that it only has values on E , allowing it to be converted into the transition rates (see Sec. S1 A). For the time-integrated case (Eq. (8)), the optimal protocol $\{R\}_{0 \leq t \leq \tau}$ can be expressed using the optimal transport matrix within $\mathcal{U}(p_{XY}^f, p_{XY}^o)$ with respect to d_E .

The transition rates R that achieve the minimum value of Eq. (9) can be expressed using the optimal transport matrix $\Pi^* \in \mathcal{U}(p_{X_{t+dt} Y_{t+dt}}, p_{X_t Y_t})$ with respect to d_E as follows:

$$R(r, r') p_{X_t Y_t}(r') dt = \begin{cases} \frac{1}{1-e^{-F}} \Pi^*(r, r') & (\Pi^*(r, r') \geq 0, \Pi^*(r', r) = 0) \\ \frac{1}{e^F - 1} \Pi^*(r', r) & (\Pi^*(r, r') = 0, \Pi^*(r', r) > 0) \end{cases} \quad (\text{S3})$$

Note that due to the unidirectional nature of optimal transport, it is never the case that both $\Pi^*(r, r') > 0$ and $\Pi^*(r', r) > 0$. Here, $F (\geq 0)$ is the thermodynamic force driving the transition on edge E , given by $F = 2 \tanh^{-1}(\dot{\mathcal{L}}_E / \dot{A}_{XY})$. From the perspective of transport, the thermodynamic force characterizes the unidirectionality of transport on edge E . For the time-integrated case (Eq. (10)), the optimal transport matrix concerning d_E within $\mathcal{U}(p_{XY}^f, p_{XY}^o)$ is used. In this case, the thermodynamic force should be taken to be a constant value $F = 2 \tanh^{-1}(\mathcal{W}_E / A_{XY})$ at each time step.

C. Remarks on the Activity Bound

Let us provide some additional remarks regarding the upper bounds on activity. These remarks are also applicable to the minimization in Sec. III. In Sec. II C 2, we set an upper bound on the activity (rate) to minimize the EP (rate). In the absence of such constraints, it is known that EP can be reduced to zero in discrete systems [S2]. However, this does not imply that dissipation can be reduced to zero in finite time. In discrete systems, if there is no limit on activity, the transition rates can be increased indefinitely, effectively achieving a quasistatic limit. Therefore, imposing an upper bound on activity allows us to consider the dynamics over a finite timescale.

On the other hand, it is possible to impose other physical constraints that compete with EP. In Ref. [S3], the dynamical state mobility is fixed (although the optimal protocol is equivalent to that of activity). In continuous systems, since the diffusion coefficient, which provides the timescale, is typically not controlled, there exists a finite lower bound on EP even without other constraints [S4, S5]. Ref. [S6] further imposes a constraint that reduces the deviation from a target trajectory in continuous systems.

Moreover, if the realized activity does not reach its upper bound in a protocol that provides the desired time evolution, it is possible to increase the activity to reduce the EP. Therefore, when discussing the minimum EP, it can be assumed that the upper bound of activity is achieved. For simplicity, we abuse the notation and use $A_{XY}(\dot{A}_{XY})$ to refer to both the upper bound of activity (rate) and the activity (rate) itself.

D. Decomposition of Time Evolution

The master equation (2) examines the probability distribution of X and Y at the same time, but it is also possible to consider probability distributions where only X or Y has partially evolved. Utilizing the bipartite nature, the probability $p_{X_{t+dt}Y_t}(x, y)$ for $X_{t+dt} = x, Y_t = y$ can be expressed as

$$\begin{aligned} p_{X_{t+dt}Y_t}(x, y) &= \left(1 - \sum_{x'(\neq x)} R_{x'x}^y dt - \sum_{y'(\neq y)} R_x^{y'y} dt\right) p_{X_tY_t}(x, y) + \sum_{x'(\neq x)} R_{xx'}^y p_{X_tY_t}(x', y) dt + \sum_{y'(\neq y)} R_x^{y'y} p_{X_tY_t}(x, y) dt \\ &= p_{X_tY_t}(x, y) + \sum_{x'(\neq x)} J_{x'x}^y dt. \end{aligned} \quad (S4)$$

Hereafter, we will ignore the $o(dt)$ terms. Similarly, for $p_{X_tY_{t+dt}}(x, y)$, we have

$$p_{X_tY_{t+dt}}(x, y) = p_{X_tY_t}(x, y) + \sum_{y'(\neq y)} J_x^{y'y} dt. \quad (S5)$$

Combining these with the master equation (2), we get

$$p_{X_{t+dt}Y_{t+dt}}(r) - p_{X_{t+dt}Y_t}(r) = p_{X_tY_{t+dt}}(r) - p_{X_tY_t}(r). \quad (S6)$$

This indicates that when the infinitesimal time evolution $p_{X_tY_t} \rightarrow p_{X_{t+dt}Y_{t+dt}}$ is given and we determine one of the partial time evolutions $p_{X_{t+dt}Y_t}$ or $p_{X_tY_{t+dt}}$, the other is automatically determined. If we specify transition rates that realize the infinitesimal time evolution $p_{X_tY_t} \rightarrow p_{X_{t+dt}Y_{t+dt}}$, the partial time evolutions Eqs. (S4)(S5) are determined. However, from $p_{X_tY_t} \rightarrow p_{X_{t+dt}Y_{t+dt}}$ alone, these cannot be determined.

Furthermore, for any subset E' of E and any probability distributions p_1, q_1, p_2, q_2 on N , the following holds:

$$\begin{cases} \mathcal{W}_{E'}(p_1, q_1) = \mathcal{O}(dt), \mathcal{W}_{E'}(p_2, q_2) = \mathcal{O}(dt), \\ p_1(r) - q_1(r) = p_2(r) - q_2(r) \ (\forall r \in N) \end{cases} \implies \mathcal{W}_{E'}(p_1, q_1) = \mathcal{W}_{E'}(p_2, q_2). \quad (S7)$$

This can be shown as follows. Let Π^* be the optimal transport matrix concerning $d_{E'}$ within $\mathcal{U}(p_1, q_1)$. We define a new transport matrix Π as

$$\Pi(r, r') = \begin{cases} \Pi^*(r, r') & (r \neq r') \\ q_2(r) - \sum_{r''(\neq r)} \Pi^*(r'', r) & (r = r') \end{cases}. \quad (S8)$$

Since the transport amount on the edge is $\mathcal{O}(dt)$, the diagonal elements are nonnegative. Thus, we have

$$\begin{aligned} \sum_{r'} \Pi(r, r') &= \sum_{r'(\neq r)} \Pi^*(r, r') + q_2(r) - \sum_{r''(\neq r)} \Pi^*(r'', r) \\ &= (p_1(r) - \Pi^*(r, r)) + q_2(r) + (\Pi^*(r, r) - q_1(r)) \\ &= p_2(r). \end{aligned}$$

In the second equality, we used the fact that $\Pi^* \in \mathcal{U}(p_1, q_1)$, and in the third equality, we used $p_1(r) - q_1(r) = p_2(r) - q_2(r)$. Therefore, $\Pi \in \mathcal{U}(p_2, q_2)$, but it is not necessarily optimal with respect to $d_{E'}$. Thus we get

$$\mathcal{W}_{E'}(p_2, q_2) \leq \sum_{r, r'} d_{E'}(r, r') \Pi(r, r') = \sum_{r, r'} d_{E'}(r, r') \Pi^*(r, r') = \mathcal{W}_{E'}(p_1, q_1).$$

The reverse inequality can be shown in exactly the same way, thus establishing Eq. (S7). Combining this with Eq. (S6), we obtain

$$\mathcal{W}_{E_X}(p_{X_{t+dt}Y_t}, p_{X_tY_t}) = \mathcal{W}_{E_X}(p_{X_{t+dt}Y_{t+dt}}, p_{X_tY_{t+dt}}), \mathcal{W}_{E_Y}(p_{X_tY_{t+dt}}, p_{X_tY_t}) = \mathcal{W}_{E_Y}(p_{X_{t+dt}Y_{t+dt}}, p_{X_{t+dt}Y_t}). \quad (S9)$$

Now, in addition to the overall time evolution $p_{X_tY_t} \rightarrow p_{X_{t+dt}Y_{t+dt}}$, we fix one partial time evolution $p_{X_tY_t} \rightarrow p_{X_{t+dt}Y_t}$ such that $\mathcal{W}_{E_X}(p_{X_{t+dt}Y_t}, p_{X_tY_t}) = \mathcal{O}(dt)$ and $\mathcal{W}_{E_Y}(p_{X_tY_{t+dt}}, p_{X_tY_t}) = \mathcal{O}(dt)$. Regarding these Wasserstein distances, the following inequality holds:

$$\mathcal{W}_{E_X}(p_{X_{t+dt}Y_t}, p_{X_tY_t}) + \mathcal{W}_{E_Y}(p_{X_tY_{t+dt}}, p_{X_tY_t}) \geq \mathcal{W}_E(p_{X_{t+dt}Y_{t+dt}}, p_{X_tY_t}). \quad (S10)$$

The equality holds when the optimal transport matrix concerning d_E in $\mathcal{U}(p_{X_{t+dt}Y_{t+dt}}, p_{X_tY_t})$ is converted into transition rates, and $p_{X_{t+dt}Y_t}$ and $p_{X_tY_{t+dt}}$ are given by the partial time evolutions based on their X and Y components.

To prove Eq. (S10), we start by considering the optimal transport matrix concerning d_{E_X} in $\mathcal{U}(p_{X_{t+dt}Y_t}, p_{X_tY_t})$, transformed to have nonzero values on the edges in E_X . We denote this matrix as Π_X^* , where the elements on E_Y are zero. Similarly, we denote the corresponding matrix for Y as Π_Y^* . From these transport matrices, we construct the overall transport matrix as

$$\Pi(r, r') = \begin{cases} \Pi_X^*(r, r') & ([r, r'] \in E_X) \\ \Pi_Y^*(r, r') & ([r, r'] \in E_Y) \\ p_{X_tY_t}(r) - \sum_{r''(\neq r)} \Pi_X^*(r'', r) & (r = r') \\ - \sum_{r''(\neq r)} \Pi_Y^*(r'', r) & (r = r') \\ 0 & (\text{otherwise}) \end{cases}. \quad (\text{S11})$$

Since the transport amount on the edges is $\mathcal{O}(dt)$, the diagonal elements are nonnegative. From Eq. (S6), we see that $\Pi \in \mathcal{U}(p_{X_{t+dt}Y_{t+dt}}, p_{X_tY_t})$, but it is not necessarily optimal with respect to d_E . Therefore, we have

$$\begin{aligned} \mathcal{W}_{E_X}(p_{X_{t+dt}Y_t}, p_{X_tY_t}) + \mathcal{W}_{E_Y}(p_{X_tY_{t+dt}}, p_{X_tY_t}) &= \sum_{r, r'} d_{E_X}(r, r') \Pi_X^*(r, r') + \sum_{r, r'} d_{E_Y}(r, r') \Pi_Y^*(r, r') \\ &= \sum_{r, r'} d_E(r, r') \Pi(r, r') \\ &\geq \mathcal{W}_E(p_{X_{t+dt}Y_{t+dt}}, p_{X_tY_t}). \end{aligned}$$

In the second equality, we used the fact that when there is a transport on the edges in E_X (E_Y), $d_E = d_{E_X} = 1$ ($d_E = d_{E_Y} = 1$). The equality holds only when Π is the optimal transport matrix with respect to d_E . Hence, if we denote the partial time evolutions induced by this optimal transport matrix as $p_{X_tY_t} \rightarrow p_{X_{t+dt}Y_t}^*, p_{X_tY_t}^*$, the following equality

$$\mathcal{W}_{E_X}(p_{X_{t+dt}Y_t}^*, p_{X_tY_t}) + \mathcal{W}_{E_Y}(p_{X_tY_{t+dt}}^*, p_{X_tY_t}) = \mathcal{W}_E(p_{X_{t+dt}Y_{t+dt}}, p_{X_tY_t}) \quad (\text{S12})$$

holds. In general, the optimal transport matrix is not unique, and X and Y components of the transport cost, $\mathcal{W}_{E_X}(p_{X_{t+dt}Y_t}^*, p_{X_tY_t})$ and $\mathcal{W}_{E_Y}(p_{X_tY_{t+dt}}^*, p_{X_tY_t})$, can vary. However, their sum always matches the overall optimal transport cost (see Fig. 6(b)).

E. Proof of Eqs. (14)(18)

In addition to the overall infinitesimal time evolution $p_{X_tY_t} \rightarrow p_{X_{t+dt}Y_{t+dt}}$, the partial time evolution $p_{X_tY_t} \rightarrow p_{X_{t+dt}Y_t}$ is fixed. For any transition rates $R_X : p_{X_tY_t} \rightarrow p_{X_{t+dt}Y_t}$, we use the transformation (S2) to convert it into a transport matrix $\Pi_X \in \mathcal{U}(p_{X_{t+dt}Y_t}, p_{X_tY_t})$. The activity rate of X can be expressed as

$$\dot{A}_X = \sum_{x \neq x', y} R_{xx'}^y p_{X_tY_t}(x', y) = \frac{1}{dt} \sum_{r \neq r'} \Pi_X(r, r') = \frac{1}{dt} \sum_{r, r'} d_{E_X}(r, r') \Pi_X(r, r'). \quad (\text{S13})$$

In this transformation, we utilized the fact that Π_X only takes nonzero values on E_X (where $d_{E_X} = 1$) or on the diagonal elements (where $d_{E_X} = 0$). On the other hand, any transport matrix in $\mathcal{U}(p_{X_{t+dt}Y_{t+dt}}, p_{X_tY_t})$ that has off-diagonal elements of $\mathcal{O}(dt)$ (as matrices without this property cannot be optimal transport matrices) can be converted into transition rates that realize $p_{X_tY_t} \rightarrow p_{X_{t+dt}Y_t}$ using the transformation (S1). Thus, Eq. (S13) holds. Therefore, the local minimum of the partial activity rate is given by

$$\min_{R_X : p_{X_tY_t} \rightarrow p_{X_{t+dt}Y_t}} \dot{A}_X = \min_{\Pi \in \mathcal{U}(p_{X_{t+dt}Y_{t+dt}}, p_{X_tY_t})} \frac{1}{dt} \sum_{r, r'} d_{E_X}(r, r') \Pi(r, r') = \frac{1}{dt} \mathcal{W}_{E_X}(p_{X_{t+dt}Y_t}, p_{X_tY_t}), \quad (\text{S14})$$

demonstrating Eq. (14).

Next, we prove Eq. (18). We will show that for a general $p_{X_{t+dt}Y_t}$ satisfying $\dot{\mathcal{L}}_{E_X} < \infty$ and $\dot{\mathcal{L}}_{E_Y} < \infty$, the inequality $\dot{\mathcal{L}}_{E_X/E} \leq \dot{\mathcal{L}}_{E_X}$ holds, and that equality can be achieved with a suitable choice of $p_{X_{t+dt}Y_t}$. Let Π_X^* be the optimal transport matrix concerning d_{E_X} in $\mathcal{U}(p_{X_{t+dt}Y_t}, p_{X_tY_t})$. Also, let Π_Y be a transport matrix in $\mathcal{U}(p_{X_tY_{t+dt}}, p_{X_tY_t})$ that can be transformed on the edges only in E_Y (though it is not necessarily optimal concerning d_{E_Y}). The matrices Π_X^* and Π_Y are transformed on the

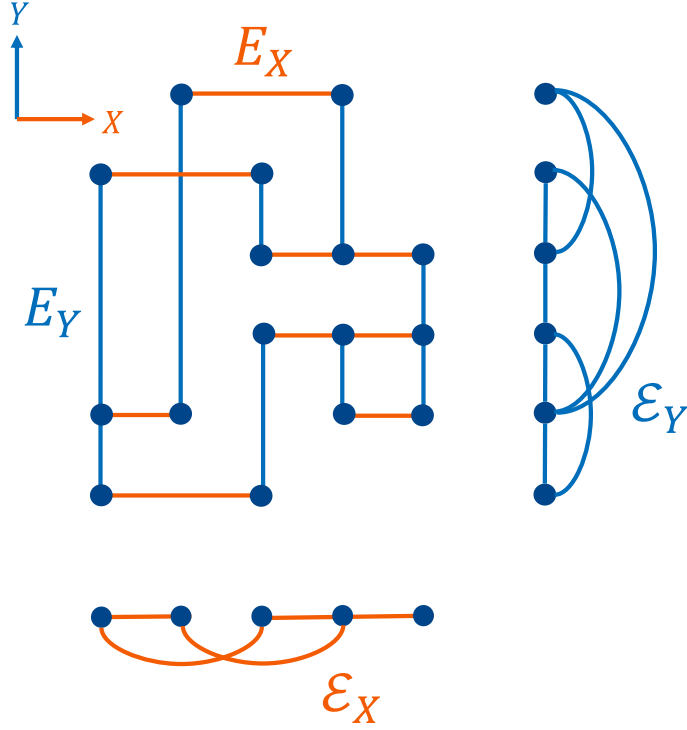


FIG. S1. Marginalization of the graph.

edges in E_X and E_Y , respectively. We construct the overall transport matrix $\Pi \in \mathcal{U}(p_{X_{t+dt}Y_{t+dt}}, p_{X_tY_t})$ from these transport matrices in the same manner as Eq. (S11). Thus, we have

$$\begin{aligned}
 \mathcal{W}_{E_X}(p_{X_{t+dt}Y_{t+dt}}, p_{X_tY_t}) &= \sum_{[r,r'] \in E_X} d_{E_X}(r, r') \Pi_X^*(r, r') \\
 &= \sum_{[r,r'] \in E_X} d_{E_X/E}(r, r') \Pi_X^*(r, r') + \sum_{[r,r'] \in E_Y} d_{E_X/E}(r, r') \Pi_Y(r, r') \\
 &= \sum_{r, r'} d_{E_X/E}(r, r') \Pi(r, r') \\
 &\geq \mathcal{W}_{E_X/E}(p_{X_{t+dt}Y_{t+dt}}, p_{X_tY_t}).
 \end{aligned} \tag{S15}$$

In the second equality, we used the fact that $d_{E_X/E} = 0$ for $[r, r'] \in E_Y$. This inequality holds for any $p_{X_{t+dt}Y_{t+dt}}$ satisfying $\dot{\mathcal{L}}_{E_X} < \infty$ and $\dot{\mathcal{L}}_{E_Y} < \infty$. Equality is achieved if and only if Π is the optimal transport matrix concerning $d_{E_X/E}$ in $\mathcal{U}(p_{X_{t+dt}Y_{t+dt}}, p_{X_tY_t})$. Combining this with Eq. (S14), when this optimal transport matrix is converted into transition rates and the system is evolved partially in time according to the X and Y components, the global minimum of the activity rate of X is realized (as stated in Eq. (18)).

F. Marginalization

Here, we consider the dynamics of only one subsystem by tracing out the information of the other subsystem. We observe that the lower bounds on activity and EP obtained in this manner are no longer tight and cannot achieve equality in general. In this section, we primarily address the marginalization to X , but the same applies when marginalizing to Y .

As a preparation, we construct the marginalized graph $G(\mathcal{N}_X, \mathcal{E}_X)$ from the original graph $G(N, E)$ as shown in Fig. S1. Formally, the set of nodes is defined as $\mathcal{N}_X := \{x | \exists y \text{ s.t. } (x, y) \in N\}$, and the set of edges is defined as $\mathcal{E}_X := \{[x, x'] | \exists y \text{ s.t. } [(x, y), (x', y)] \in E_X\}$. From the time evolution of the total system $p_{X_tY_t} \rightarrow p_{X_{t+dt}Y_{t+dt}}$, the time evolution of the subsystem $p_{X_t} \rightarrow p_{X_{t+dt}}$ is uniquely determined. This is realized by the transition rates on \mathcal{E}_X .

On the other hand, let us fix a partial time evolution $p_{X_t Y_t} \rightarrow p_{X_{t+dt} Y_t}$. Denote the optimal transport matrix concerning d_{E_X} within $\mathcal{U}(p_{X_{t+dt} Y_t}, p_{X_t Y_t})$, which has nonzero values on the edges E_X , as Π_X^* . The transport matrix obtained by tracing out the Y component of Π_X^* is denoted as π_X . Specifically, this transport matrix is defined as $\pi_X(x, x') := \sum_y \Pi_X^*((x, y), (x', y))$. A simple calculation shows that $\pi_X \in \mathcal{U}(p_{X_{t+dt}}, p_{X_t})$, but it is not necessarily optimal with respect to the cost function d_{E_X} . Therefore,

$$\begin{aligned} \mathcal{W}_{E_X}(p_{X_{t+dt} Y_t}, p_{X_t Y_t}) &= \sum_{r, r'} d_{E_X}(r, r') \Pi_X^*(r, r') \\ &= \sum_{x, x', y} d_{E_X}((x, y), (x', y)) \Pi_X^*((x, y), (x', y)) \\ &= \sum_{x, x'} d_{E_X}(x, x') \pi_X(x, x') \\ &\geq \mathcal{W}_{E_X}(p_{X_{t+dt}}, p_{X_t}). \end{aligned} \quad (\text{S16})$$

In the third equality, we used the fact that the summand is nonzero only when $[(x, y), (x', y)] \in E_X$, at which point $d_{E_X}((x, y), (x', y)) = d_{E_X}(x, x') = 1$. The equality in Eq. (S16) holds if and only if π_X is the optimal transport matrix. However, the constraints after marginalization do not need to consider the correlation with Y , so in general, there exists a transport matrix more optimal than π_X concerning d_{E_X} . Therefore, the equality generally cannot be achieved.

The inequality (S16) holds for any $p_{X_{t+dt} Y_t}$ that satisfies $\dot{\mathcal{L}}_{E_X} < \infty$ and $\dot{\mathcal{L}}_{E_Y} < \infty$. This includes the partial time evolution that gives $\dot{\mathcal{L}}_{E_X/E}$. Therefore, denoting $\dot{\mathcal{L}}_{E_X} := \mathcal{W}_{E_X}(p_{X_{t+dt}}, p_{X_t})/dt$, we have $\dot{\mathcal{L}}_{E_X/E} \geq \dot{\mathcal{L}}_{E_X}$. Combining this with Eq. (20), for an infinitesimal time evolution $p_{X_t Y_t} \rightarrow p_{X_{t+dt} Y_{t+dt}}$, when the upper bound of the partial activity rate of X is \dot{A}_X , the lower bound of the minimum partial EP rate is given by:

$$\min_{\substack{R: p_{X_t Y_t} \rightarrow p_{X_{t+dt} Y_{t+dt}} \\ \dot{A}_X \text{ fixed}}} \dot{\Sigma}_X \geq 2 \dot{\mathcal{L}}_{E_X} \tanh^{-1} \left(\frac{\dot{\mathcal{L}}_{E_X}}{\dot{A}_X} \right). \quad (\text{S17})$$

This lower bound does not use information about the correlation with Y .

In addition, this lower bound can be obtained even when considering the marginalized dynamics from the beginning. Using the transition rates R that realize the infinitesimal time evolution $p_{X_t Y_t} \rightarrow p_{X_{t+dt} Y_{t+dt}}$, we define the marginalized transition rates for X as $\mathcal{R}_{xx'} := \sum_y R_{xx'}^y p_{X_t Y_t}(x', y) / p_{X_t}(x')$. These transition rates realize the infinitesimal time evolution $p_{X_t} \rightarrow p_{X_{t+dt}}$. Furthermore, its activity rate matches the partial activity rate of X given by the original R : $\dot{A}_X = \sum_{x \neq x'} \mathcal{R}_{xx'} p_{X_t}(x')$. Regarding the partial EP rate, by the log-sum inequality, we have

$$\begin{aligned} \dot{\Sigma}_X &= \sum_{x > x', y} (R_{xx'}^y p_{X_t Y_t}(x', y) - R_{x'x}^y p_{X_t Y_t}(x, y)) \ln \frac{R_{xx'}^y p_{X_t Y_t}(x', y)}{R_{x'x}^y p_{X_t Y_t}(x, y)} \\ &\geq \sum_{x > x'} (\mathcal{R}_{xx'} p_{X_t}(x') - \mathcal{R}_{x'x} p_{X_t}(x)) \ln \frac{\mathcal{R}_{xx'} p_{X_t}(x')}{\mathcal{R}_{x'x} p_{X_t}(x)}. \end{aligned} \quad (\text{S18})$$

The rightmost term represents the EP rate generated by the transition rates \mathcal{R} during the infinitesimal time evolution $p_{X_t} \rightarrow p_{X_{t+dt}}$. Applying the discussion from Sec. II C to this time evolution, the minimum value of the rightmost term is given by the right-hand side of Eq. (S17).

S2. SUPPLEMENTAL TO SECTION IV

A. Definition of the Pareto Front

We define the Pareto front \mathcal{F}_C for the feasible region $K_C (\neq \emptyset)$, which is the set of all feasible cost function pairs $C = (C_X, C_Y)$. A pair (C_X, C_Y) is said to dominate another pair (C'_X, C'_Y) if either $C_X < C'_X, C_Y \leq C'_Y$, or $C_X \leq C'_X, C_Y < C'_Y$. This is denoted as $(C_X, C_Y) \prec (C'_X, C'_Y)$. Conversely, if (C'_X, C'_Y) is not dominated by (C_X, C_Y) , it is denoted as $(C_X, C_Y) \not\prec (C'_X, C'_Y)$. The Pareto front \mathcal{F}_C is the set of elements in K_C that are not dominated by any other element in K_C . Specifically, it is defined as:

$$\mathcal{F}_C := \{(C_X, C_Y) \in K_C | \forall (C'_X, C'_Y) \in K_C, (C'_X, C'_Y) \not\prec (C_X, C_Y)\} \quad (\text{S19})$$

(see Fig. 6(a)). When comparing an element on this front with any other element in K_C , if one cost can be decreased, the other cost must inevitably increase. The same applies to sets of three or more dimensions.

B. Minimization of Convex Combination of Partial Activities

The infinitesimal time evolution $p_{X_t Y_t} \rightarrow p_{X_{t+dt} Y_{t+dt}}$ of the total system is fixed. For any transition rates $R : p_{X_t Y_t} \rightarrow p_{X_{t+dt} Y_{t+dt}}$, we use the transformation (S2) to convert it into a transport matrix $\Pi \in \mathcal{U}(p_{X_{t+dt} Y_{t+dt}}, p_{X_t Y_t})$. The convex combination of the partial activity rates can be expressed as:

$$\begin{aligned} s\dot{A}_X + (1-s)\dot{A}_Y &= s \sum_{x \neq x', y} R_{xx'}^y p_{X_t Y_t}(x', y) + (1-s) \sum_{y \neq y', x} R_x^{yy'} p_{X_t Y_t}(x, y) \\ &= s \frac{1}{dt} \sum_{[r, r'] \in E_X} \Pi(r, r') + (1-s) \frac{1}{dt} \sum_{[r, r'] \in E_Y} \Pi(r, r') \\ &= \frac{1}{dt} \sum_{r, r'} d_{E_X: E_Y}^s(r, r') \Pi(r, r'). \end{aligned} \quad (\text{S20})$$

In this transformation, we used the fact that Π takes nonzero values only on E_X (where $d_{E_X: E_Y}^s = s$), E_Y (where $d_{E_X: E_Y}^s = 1-s$), and diagonal elements (where $d_{E_X: E_Y}^s = 0$). On the other hand, any transport matrix in $\mathcal{U}(p_{X_{t+dt} Y_{t+dt}}, p_{X_t Y_t})$, which has off-diagonal elements of order $\mathcal{O}(dt)$, can be converted back into the transition rates R that realize $p_{X_t Y_t} \rightarrow p_{X_{t+dt} Y_{t+dt}}$ using the transformation (S1). Thus, Eq. (S20) holds. Therefore, the minimum value of the convex combination of the partial activity rates is given by:

$$\begin{aligned} \min_{R: p_{X_t Y_t} \rightarrow p_{X_{t+dt} Y_{t+dt}}} [s\dot{A}_X + (1-s)\dot{A}_Y] &= \min_{\Pi \in \mathcal{U}(p_{X_{t+dt} Y_{t+dt}}, p_{X_t Y_t})} \frac{1}{dt} \sum_{r, r'} d_{E_X: E_Y}^s(r, r') \Pi(r, r') \\ &= \frac{1}{dt} \mathcal{W}_{E_X: E_Y}^s(p_{X_{t+dt} Y_{t+dt}}, p_{X_t Y_t}). \end{aligned} \quad (\text{S21})$$

Since $\mathcal{W}_{E_X: E_Y}^s$ satisfies the triangle inequality, the minimum value of $s\dot{A}_X + (1-s)\dot{A}_Y$ is $\mathcal{W}_{E_X: E_Y}^s(p_{X_Y}^f, p_{X_Y}^o)$ (cf. Eq. (19)).

C. Shape of \mathcal{F}_A

Similar to Eq. (S3), the protocols that give \mathcal{F}_A can be constructed from the optimal transport matrices concerning $d_{E_X: E_Y}^s$ within $\mathcal{U}(p_{X_Y}^f, p_{X_Y}^o)$. Equation (27) is a linear programming problem, and since the transport polytope $\mathcal{U}(p, q)$ is bounded, an optimal solution always exists. Furthermore, this solution can be expressed as a vertex of the transport polytope [S7]. If the vertex solution has values outside E (and diagonal elements), it can be transformed into a vertex solution that only has values on E . Therefore, when seeking \mathcal{F}_A , which considers the components of the transport cost, we only need to consider the vertex solutions that have values solely on E .

The shape of \mathcal{F}_A can be understood from the perspective of vertex solutions to the optimal transport problem. For the interval of s corresponding to a vertex (excluding the endpoints), the optimal transport problem's vertex solution remains the same, or there are multiple vertex solutions with the same transport cost components for X and Y . Conversely, for s corresponding to an edge, multiple vertex solutions with different transport cost components exist, providing the vertices at both ends of the edge. The convex combination of these vertex solutions also forms an optimal solution, covering all points on the edge. Different vertices correspond to different vertex solutions. The number of vertices is at most the number of vertices of the transport polytope (at most $|N|^{2(|N|-1)}$ [S8]). Therefore, \mathcal{F}_A will not have curves consisting of infinitely many edges and vertices.

D. Convexity of K_A

In the case of infinitesimal time evolution, we consider the feasible set of partial activity rates $K_{\dot{A}}$. The same can be derived for finite time. By lowering the partial EP rate, the partial activity rates for X and Y can be independently increased without bound, so we only need to focus on the lower left part of $K_{\dot{A}}$. Consider any two points from $K_{\dot{A}}$. These

points can be represented as $(\dot{\mathcal{L}}_{E_X}(p_{X_{t+dt}Y_t}), \dot{\mathcal{L}}_{E_Y}(p_{X_{t+dt}Y_t}))$ and $(\dot{\mathcal{L}}_{E_X}(p'_{X_{t+dt}Y_t}), \dot{\mathcal{L}}_{E_Y}(p'_{X_{t+dt}Y_t}))$ because, by construction, for any point (\dot{A}_X, \dot{A}_Y) in $K_{\dot{A}}$, there exist $p_{X_{t+dt}Y_t}, F_X \geq 0, F_Y \geq 0$ such that $\dot{A}_X = \coth(F_X/2)\dot{\mathcal{L}}_{E_X}(p_{X_{t+dt}Y_t})$ and $\dot{A}_Y = \coth(F_Y/2)\dot{\mathcal{L}}_{E_Y}(p_{X_{t+dt}Y_t})$. The convex combination using $(\dot{\mathcal{L}}_{E_X}(p_{X_{t+dt}Y_t}), \dot{\mathcal{L}}_{E_Y}(p_{X_{t+dt}Y_t}))$ will dominate the convex combination using (\dot{A}_X, \dot{A}_Y) . Therefore, when seeking the optimal pair of partial activity rates, we only need to consider $(\dot{\mathcal{L}}_{E_X}(p_{X_{t+dt}Y_t}), \dot{\mathcal{L}}_{E_Y}(p_{X_{t+dt}Y_t}))$.

To show that $K_{\dot{A}}$ is convex, we need to demonstrate that for any λ ($0 \leq \lambda \leq 1$),

$$\left(\lambda \dot{\mathcal{L}}_{E_X}(p_{X_{t+dt}Y_t}) + (1-\lambda)\dot{\mathcal{L}}_{E_X}(p'_{X_{t+dt}Y_t}), \lambda \dot{\mathcal{L}}_{E_Y}(p_{X_{t+dt}Y_t}) + (1-\lambda)\dot{\mathcal{L}}_{E_Y}(p'_{X_{t+dt}Y_t}) \right) \in K_{\dot{A}}. \quad (\text{S22})$$

The optimal transport matrices concerning d_{E_X} in $\mathcal{U}(p_{X_{t+dt}Y_t}, p_{X_tY_t})$ and $\mathcal{U}(p'_{X_{t+dt}Y_t}, p_{X_tY_t})$ are taken to yield a convex combination with coefficient λ . This will be an element of $\mathcal{U}(\lambda p_{X_{t+dt}Y_t} + (1-\lambda)p'_{X_{t+dt}Y_t}, p_{X_tY_t})$, and the transport cost will be $\lambda \dot{\mathcal{L}}_{E_X}(p_{X_{t+dt}Y_t}) + (1-\lambda)\dot{\mathcal{L}}_{E_X}(p'_{X_{t+dt}Y_t})$. However, this is not necessarily optimal concerning d_{E_X} . Therefore,

$$\lambda \dot{\mathcal{L}}_{E_X}(p_{X_{t+dt}Y_t}) + (1-\lambda)\dot{\mathcal{L}}_{E_X}(p'_{X_{t+dt}Y_t}) \geq \dot{\mathcal{L}}_{E_X}(\lambda p_{X_{t+dt}Y_t} + (1-\lambda)p'_{X_{t+dt}Y_t}). \quad (\text{S23})$$

The same reasoning applies for d_{E_Y} , so

$$\lambda \dot{\mathcal{L}}_{E_Y}(p_{X_{t+dt}Y_t}) + (1-\lambda)\dot{\mathcal{L}}_{E_Y}(p'_{X_{t+dt}Y_t}) \geq \dot{\mathcal{L}}_{E_Y}(\lambda p_{X_{t+dt}Y_t} + (1-\lambda)p'_{X_{t+dt}Y_t}) \quad (\text{S24})$$

holds. Thus, by adjusting the thermodynamic force, we can achieve Eq. (S22).

We focus on the edge of the Pareto front with the slope $-s/(1-s)$. There exist multiple optimal transportation matrices for $\mathcal{W}_{E_X:E_Y}^s(p_{X_{t+dt}Y_{t+dt}}, p_{X_tY_t})$ where the X and Y components of the transportation cost differ. By selecting two of these transportation matrices and converting them into transition rates, we obtain probability distributions $p_{X_{t+dt}Y_t}$ and $p'_{X_{t+dt}Y_t}$ which represent the partial time evolution of X . For any λ such that $0 \leq \lambda \leq 1$, the equality conditions of Eq. (S23) and (S24) hold. If they did not hold, it would imply that $s\dot{A}_X + (1-s)\dot{A}_Y$ could be made smaller than $\mathcal{W}_{E_X:E_Y}^s(p_{X_{t+dt}Y_{t+dt}}, p_{X_tY_t})/dt$, which is a contradiction. Therefore, by taking a convex combination in this manner, any point on the edge of the Pareto front can be realized.

S3. NOMENCLATURE

Here, we list and briefly explain the symbols that appear in this paper (see Table S1).

-
- [S1] A. Dechant, Minimum entropy production, detailed balance and wasserstein distance for continuous-time markov processes, *J. Phys. A* **55**, 094001 (2022).
 - [S2] P. Muratore-Ginanneschi, C. Mejía-Monasterio, and L. Peliti, Heat release by controlled continuous-time markov jump processes, *Journal of Statistical Physics* **150**, 181 (2013).
 - [S3] T. Van Vu and K. Saito, Thermodynamic unification of optimal transport: Thermodynamic uncertainty relation, minimum dissipation, and thermodynamic speed limits, *Phys. Rev. X* **13**, 011013 (2023).
 - [S4] E. Aurell, C. Mejía-Monasterio, and P. Muratore-Ginanneschi, Optimal protocols and optimal transport in stochastic thermodynamics, *Phys. Rev. Lett.* **106**, 250601 (2011).
 - [S5] E. Aurell, K. Gawędzki, C. Mejía-Monasterio, R. Mohayaei, and P. Muratore-Ginanneschi, Refined second law of thermodynamics for fast random processes, *Journal of statistical physics* **147**, 487 (2012).
 - [S6] K. Proesmans, Precision-dissipation trade-off for driven stochastic systems, *Communications Physics* **6**, 226 (2023).
 - [S7] J. Nocedal and S. J. Wright, *Numerical optimization* (Springer, 1999).
 - [S8] M. Dyer, H. M. L. Stougie, and M. Cryan, Random walks on the vertices of transportation polytopes with constant number of sources, in *Proceedings of the Fourteenth Annual ACM-SIAM Symposium on Discrete Algorithms* (SIAM, 2003) p. 330.

TABLE S1. Nomenclature.

A_{XY}, A_X, A_Y	activity and upper bound of activity
$C = (C_X, C_Y)$	cost function in multiobjective optimization
\mathcal{C}	free energy's dependence on ligand concentration
$d_E, d_{E_X/E}, d_{E_X:E_Y}^s$	cost function in optimal transport problem
E, E_X, E_Y	edge set
$\mathcal{E}_X, \mathcal{E}_Y$	marginalized edge set
f_X, f_Y	Fermi distribution
F, F_X, F_Y	thermodynamic force
$\mathcal{F}_C, \mathcal{F}_A, \mathcal{F}_\Sigma$	Pareto front
G	graph
I_{XY}	mutual information
\dot{I}_X, \dot{I}_Y	information flow
$J_{xx'}^y, J_x^{yy'}$	probability current
k_B, k_R, k_Y	reaction rates in <i>E.coli</i> chemotaxis
K_C, K_A, K_Σ	feasible region
$l_E(P)$	the number of edges in E traversed by P
$\mathcal{L}_E, \mathcal{L}_{E_X}, \mathcal{L}_{E_Y}, \mathcal{L}_{E_X/E}, \mathcal{L}_{E_Y/E}$	trajectory length measured by the Wasserstein distance
N	node set
$\mathcal{N}_X, \mathcal{N}_Y$	marginalized node set
p, q	probability distribution
$p_{X_t Y_t}, p_{X_{t+dt} Y_{t+dt}}, p_{XY}^o, p_{XY}^f$	probability distribution of the total system
$p_{X_{t+dt} Y_t}, p_{X_t Y_{t+dt}}$	partially evolved probability distribution
$p_{X_t}, p_{X_{t+dt}}, p_{Y_t}, p_{Y_{t+dt}}$	probability distribution of the subsystem
$\{p_{X_t Y_t}\}_{0 \leq t \leq \tau}, \{p_{X_{t+dt} Y_t}\}_{0 \leq t \leq \tau}$	trajectory of time evolution
P	path on graph
r	state of the total system
R, R_X	transition rates
$\{R\}_{0 \leq t \leq \tau}, \{R_X\}_{0 \leq t \leq \tau}$	protocol
\mathcal{R}	marginalized transition rate
s	ratio in convex combination
t	time
\mathcal{T}	total variation distance
U	interaction energy between the quantum dots
\mathcal{U}	set of transport matrix
\mathcal{W}_E	Wasserstein distance (the optimal transport cost regarding d_E)
$\mathcal{W}_{E_X/E}$	Wasserstein pseudo distance (the optimal transport cost regarding $d_{E_X/E}$)
$\mathcal{W}_{E_X:E_Y}^s$	the optimal transport cost regarding $d_{E_X:E_Y}^s$
x, y	state of the subsystem
X, Y	subsystem
β_X, β_Y	inverse temperature of reservoir
γ_X, γ_Y	coupling strength to reservoir
ϵ	infinitesimal amount
ϵ_X, ϵ_Y	energy level of quantum dot
λ	Lagrange multiplier
μ_X, μ_Y	chemical potential of reservoir
π	marginalized transport matrix
Π	transport matrix
$\Sigma_{XY}, \Sigma_X, \Sigma_Y$	entropy production
$\Sigma_X^{\text{ap}}, \Sigma_Y^{\text{ap}}$	apparent entropy production
τ	operation time of the process
χ	bias in methylation and demethylation reactions